nature

https://doi.org/10.1038/s41586-023-05697-2

Accelerated Article Preview

Spike and nsp6 are key determinants of SARS-CoV-2 Omicron BA.1 attenuation

Received: 16 March 2022

Accepted: 4 January 2023

Accelerated Article Preview

Cite this article as: Chen, D.-Y. et al. Spike and nsp6 are key determinants of SARS-CoV-2 Omicron BA.1 attenuation. *Nature* https://doi.org/10.1038/s41586-023-05697-2 (2023)

Da-Yuan Chen, Chue Vin Chin, Devin Kenney, Alexander H. Tavares, Nazimuddin Khan, Hasahn L. Conway, GuanQun Liu, Manish C. Choudhary, Hans P. Gertje, Aoife K. O'Connell, Scott Adams, Darrell N. Kotton, Alexandra Herrmann, Armin Ensser, John H. Connor, Markus Bosmann, Jonathan Z. Li, Michaela U. Gack, Susan C. Baker, Robert N. Kirchdoerfer, Yachana Kataria, Nicholas A. Crossland, Florian Douam & Mohsan Saeed

Spike and nsp6 are key determinants of SARS-CoV-2 Omicron BA.1 attenuation

Da-Yuan Chen[1,2*], Chue Vin Chin[1,2*], Devin Kenney[2,3], Alexander H. Tavares[1,2], Nazimuddin Khan[1,2], Hasahn L. Conway[1,2], GuanQun Liu[4], Manish C. Choudhary[5,6], Hans P. Gertje[2], Aoife K. O'Connell[2], Scott Adams[2,3], Darrell N. Kotton[7,8], Alexandra Herrmann[9], Armin Ensser[9], John H. Connor[2,3], Markus Bosmann[8,10,11], Jonathan Z. Li[5,6], Michaela U. Gack[4], Susan C. Baker[12], Robert N. Kirchdoerfer[13], Yachana Kataria[11], Nicholas A. Crossland[2,11], Florian Douam[2,3], Mohsan Saeed[1,2#]

1. Department of Biochemistry, Boston University Chobanian and Avedisian School of Medicine, Boston, MA, USA
2. National Emerging Infectious Diseases Laboratories, Boston University, Boston, MA, USA
3. Department of Microbiology, Boston University Chobanian and Avedisian School of Medicine, Boston, MA, USA
4. Florida Research and Innovation Center, Cleveland Clinic, Port St. Lucie, FL, USA
5. Brigham and Women's Hospital, Boston, MA, USA
6. Harvard Medical School, Cambridge, MA, USA
7. Center for Regenerative Medicine of Boston University and Boston Medical Center, Boston, MA, USA
8. The Pulmonary Center and Department of Medicine, Boston University Chobanian and Avedisian School of Medicine, Boston, MA, USA

9. Institute of Clinical and Molecular Virology, University Hospital Erlangen, Friedrich-Alexander Universität Erlangen-Nürnberg, Erlangen, Germany

10. Department of Pathology and Laboratory Medicine, Boston University Chobanian and Avedisian School of Medicine, MA, USA

11. Center for Thrombosis and Hemostasis, University Medical Center of the Johannes Gutenberg-University, Mainz, Germany

12. Department of Microbiology and Immunology, and Infectious Disease and Immunology Research Institute, Stritch School of Medicine, Loyola University, Chicago, Maywood, IL, USA

13. Department of Biochemistry, College of Agricultural and Life Sciences, University of Wisconsin-Madison, Madison, WI, USA

*Equal contribution

#Correspondence: msaeed1@bu.edu

The SARS-CoV-2 Omicron variant is more immune-evasive and less virulent than other major viral variants recognized to date[1-12]. Omicron spike (S), with an unusually large number of mutations, is considered the major driver of these phenotypes. We generated chimeric recombinant SARS-CoV-2 encoding the S gene of Omicron (BA.1 lineage) in the

backbone of an ancestral SARS-CoV-2 isolate and compared this virus with the naturally circulating Omicron variant. The Omicron S-bearing virus robustly escaped vaccine-induced humoral immunity, mainly due to mutations in the receptor-binding motif (RBM), yet unlike naturally occurring Omicron, efficiently replicated in cell lines and primary-like distal lung cells. Similarly, in K18-hACE2 mice, although Omicron S-carrying virus caused less severe disease compared to the ancestral virus, it failed to achieve the attenuation level of Omicron. Further investigation showed that mutating nsp6 in addition to S was sufficient to recapitulate the attenuated phenotype of Omicron. This indicates that while the vaccine escape of Omicron is driven by mutations in S, the pathogenicity of Omicron is determined by mutations both in and outside of S.

As of December 2022, the successive waves of the coronavirus disease 2019 (COVID-19) pandemic have been driven by five major SARS-CoV-2 variants, called variants of concern (VOC); Alpha (B.1.1.7), Beta (B.1.351), Gamma (P.1), Delta (B.1.617.2 and AY lineages), and Omicron (BA lineages)[13]. Omicron is the most recently recognized VOC that was first documented in South Africa, Botswana, and in a traveler from South Africa in Hong Kong in November 2021 (GISAID ID: EPI_ISL_7605742)[14,15]. It quickly swept through the world, displacing the previously dominant Delta variant within weeks and accounting for the majority of new SARS-CoV-2 infections by January 2022[16-18]. At least five lineages of Omicron have so far been identified: BA.1, BA.2, BA.3, BA.4, and BA.5. BA.1 (hereinafter referred to as Omicron) exhibits a remarkable escape from infection- and vaccine-induced humoral immunity[3,19]. Further, it is less virulent than other VOCs in humans and *in vivo* models of infection[4,5,7,11,12,20]. Omicron differs from the prototype SARS-CoV-2 isolate, Wuhan-Hu-1, by 59 amino acids; 37 of these changes are in the S protein, raising the possibility that S is at the heart of Omicron's pathogenic and antigenic behavior.

Spike mutations influence Omicron replication

The Omicron S protein carries 30 amino acid substitutions, 6 deletions, and one three-amino acid-long insertion compared to Wuhan-Hu-1 (**Extended Data Fig. 1**). Twenty-five of these changes are unique to Omicron relative to other VOCs, although some of them have been reported in waste water and minor SARS-CoV-2 variants[21,22]. To test the role of the S protein in Omicron phenotype, we generated a chimeric recombinant virus containing the S gene of Omicron (USA-lh01/2021) and all other genes of a D614G-containing ancestral SARS-CoV-2 (GISAID EPI_ISL_2732373)[23] (**Extended Data Fig. 2a**). This chimeric virus, named Omi-S, we made by employing a modified form of circular polymerase extension reaction (CPER) (**Extended Data Fig. 2b**)[24] that yielded highly concentrated virus stocks, containing 0.5-5 x 10^6 plaque-forming units (PFU) per ml, from transfected cells within two days of transfection (**Extended Data Fig. 2c,d**), obviating the need for additional viral amplification.

We first compared the infection efficiency of Omi-S with the ancestral virus [also generated by CPER; hereinafter referred to as wild-type (WT)] and an Omicron isolate (USA-lh01/2021) in cell culture (**Fig. 1a**). For this, we infected ACE2/TMPRSS2/Caco-2 and Vero E6 cells with Omi-S, WT, and Omicron at a multiplicity of infection (MOI) of 0.01 and monitored viral propagation by flow cytometry and plaque formation assay. The WT virus and Omi-S spread rapidly in ACE2/TMPRSS2/Caco-2 cells, yielding 89% and 80% infected cells, respectively, at 24 hours post-infection (hpi) (**Fig. 1b**). In contrast, Omicron replicated slower, leading to 48% infected cells at 24 hpi. A similar pattern was seen in Vero E6 cells, where 60% and 41% of cells were positive for WT and Omi-S, respectively, at 48 hpi, as opposed to 10% for Omicron (**Fig. 1c**). The plaque assay showed that although both Omi-S and Omicron produced lower levels of infectious virus particles compared with WT, the viral titer of Omi-S was significantly higher than that of Omicron.

In ACE2/TMPRSS2/Caco-2 cells, Omi-S produced 5.1-fold (p = 0.0006) and 5.5-fold (p = 0.0312) more infectious particles than Omicron at 12 hpi and 24 hpi, respectively (**Fig. 1d**). Similarly, in Vero E6 cells, the infectious virus titers of Omi-S were 17-fold (p = 0.0080) and 11-fold (p = 0.0078) higher than that of Omicron at 24 hpi and 48 hpi, respectively (**Fig. 1e**). The difference between viruses became less obvious at later time points due to higher cytotoxicity caused by Omi-S compared to Omicron (**Extended Data Fig. 3a**).

Increased replication efficiency of Omi-S relative to Omicron was preserved when tested at varying MOIs (**Extended Data Fig. 3b**). We further confirmed the fitness advantage of Omi-S over Omicron by a direct competition assay. For this, we first generated recombinant Omicron (rOmicron), which, in our cell culture assays, mimicked the replication kinetics of natural Omicron (**Extended Data Fig. 4**). Next, we created mCherry-containing Omi-S and mNeonGreen-containing Omicron, and inoculated ACE2/TMPRSS2/Caco-2 cells with these viruses mixed at a 1:1 ratio. Flow cytometric analysis of infected cells at various times of infection demonstrated a clear replication superiority of Omi-S/mCherry over Omicron/mNeonGreen (**Fig. 1f**). Finally, the higher infection efficiency of Omi-S was also reflected in the plaque size; while WT virus produced the largest plaques (~ 4.1 mm), the size of Omi-S plaques (~2.2 mm) was 2-fold (p < 0.0001) larger than that of Omicron plaques (~1.1 mm) (**Fig. 1g**). These results indicate that although mutations in the S protein influence the infection efficiency of Omicron, they do not fully explain the Omicron phenotype.

Several lines of evidence indicated that the S protein incorporated into Omi-S behaved the same way as in natural Omicron. For instance, as previously published[20,25], Omicron S was poorly cleaved compared to that of WT virus; while 71% of S in WT virions was in the cleaved form, only 45% and 47% was cleaved in Omi-S and Omicron, respectively (**Extended Data Fig. 5a**). The

same pattern of S cleavage was evident in virus-infected cells (WT, 63% cleaved; Omi-S, 33% cleaved; Omicron, 42% cleaved) (**Extended Data Fig. 5b**). These experiments also revealed that Omicron S was inefficiently incorporated into virus particles compared to WT S (S to nucleocapsid (N) ratio: 3.40 for WT virus, 1.91 for Omi-S, and 2.04 for Omicron) (**Extended Data Fig. 5a**). Similarly, both Omi-S and Omicron produced smaller syncytia compared to the WT virus, an observation that has previously been reported for Omicron[20,26] (**Extended Data Fig. 5c)**. Finally, consistent with the published literature[25], Omi-S and Omicron demonstrated preference for cathepsin-mediated entry, as reflected by their higher sensitivity to the cathepsin inhibitor E64d (**Extended Data Fig. 6**).

We next compared replication kinetics of WT, Omi-S, and Omicron in lung epithelial cells, which form a major viral replication site in patients with COVID-19[27,28]. Accordingly, we employed human induced pluripotent stem cell-derived lung alveolar type 2 epithelial (iAT2) cells. AT2 cells represent an essential cell population in the distal lung and constitute one of the primary targets of SARS-CoV-2 infection[28,29]. We infected iAT2 cells, grown as an air-liquid interface (ALI) culture, at an MOI of 2.5 and monitored the secretion of viral progeny on the apical side of cells at 48 hpi and 96 hpi. In congruence with the results obtained from cell lines, WT virus produced the highest levels of infectious virus particles (**Fig. 1h**). Among the Omi-S and Omicron, the former yielded ~5-fold (p = 0.0008) higher infectious viral titer at 48 hpi. The viral titers for WT and Omi-S decreased at 96 hpi compared to 48 hpi due to the cytopathic effect (CPE) of infection. However, no CPE was seen for Omicron, leading to sustained production of infectious virions. Overall, these results corroborate the conclusion that mutations in S do not fully account for the attenuated replication capacity of Omicron in cell culture.

Spike has a minimal role in Omicron pathogenicity in mice

To examine if Omi-S exhibits higher *in vivo* fitness compared with Omicron, we investigated the infection outcome of Omi-S relative to WT SARS-CoV-2 and Omicron in K18-hACE2 mice. In agreement with the published literature[4,30], intranasal inoculation of mice (aged 12-20 weeks) with Omicron (10^4 PFU per animal) caused no significant weight loss, whereas inoculation with WT virus triggered a rapid decrease in body weight with all animals losing over 20% of their initial body weight by 8 days post-infection (dpi) (**Fig. 2a**). Importantly, 80% of animals infected with Omi-S also lost over 20% of their body weight by 9 dpi (**Fig. 2a and Extended Data Fig. 7a**). The evaluation of clinical scores (a cumulative measure of weight loss, abnormal respiration, aberrant appearance, reduced responsiveness, and altered behavior) also revealed a similar pattern; while Omicron-infected mice displayed little to no signs of clinical illness, the health of those infected with WT and Omi-S rapidly deteriorated, with the former inflicting a more severe disease (p = 0.0102) (**Fig. 2b and Extended Data Fig. 7b**). Since SARS-CoV-2 causes fatal infection in K18-hACE2 mice[4], we leveraged this observation to compare the animal survival after viral infection. Agreeing with the results of body-weight loss and clinical score, WT and Omi-S caused mortality rates of 100% (6/6) and 80% (8/10), respectively. In contrast, all animals infected with Omicron survived (**Fig. 2c**). These findings, which are consistent with a recent publication[31], indicate that the S protein is not the exclusive determinant of Omicron's pathogenicity in K18-hACE2 mice.

Next, we compared the propagation of Omi-S with Omicron and WT SARS-CoV-2 in the lungs and nasal turbinates of K18-hACE2 mice. The mice (12-20 weeks old) were intranasally challenged with 10^4 PFU (7 mice per virus), and viral titers in mice lungs were measured at 2 and 4 dpi. Consistent with *in vitro* findings, the infectious virus titer in the lungs of WT-infected mice was higher than that detected in mice infected with other two viruses (**Fig. 2d**). Notably however, Omi-S-infected mice produced 30-fold (p = 0.0286) more infectious virus particles compared with

Omicron-infected mice at 2 dpi. The titer decreased at 4 dpi for WT- and Omi-S-infected mice, yet it showed an increasing trend for Omicron-infected animals, pointing to the possibility of mild but persistent infection by Omicron in K18-hACE2 mice. All three variants recovered from the lungs of mice maintained the same plaque size phenotype as the original inoculum, indicating that replication in mice had no detectable effect on genotypes of these viruses (data not shown).

To evaluate the viral pathogenicity in lungs and nasal turbinates of K18-hACE2 mice, we performed histopathological analysis of these tissues at 2 dpi. As previously reported[4,32], an extensive near-diffused immunoreactivity of the SARS-CoV-2 N protein was detected in lung alveoli of mice infected with WT virus (**Fig. 2e**). In contrast, Omi-S and Omicron infection produced localized foci of alveolar staining with fewer foci for Omicron compared with Omi-S. The most striking phenotype was seen in bronchiolar epithelium, where Omi-S caused pronounced, routinely circumferential infection, with around 10-15% of bronchioles being positive for viral N protein at 2 dpi, whereas only 3-5% of bronchioles were N-positive for Omicron (**Fig. 2f**). WT virus infected around 1% of bronchioles and in all cases only included a single isolated epithelial cell per bronchiole. Further, bronchiolar infection was associated with epithelial necrosis in Omi-S-infected mice, as determined through serial hematoxylin and eosin (H&E) section analysis, whereas no histological evidence of airway injury was observed in Omicron- or WT-infected mice (**Extended Data Fig. 8a,b**). The nasal turbinates of mice inoculated with WT and Omi-S viruses both contained abundant SARS-CoV-2-positive cells affiliated with overt cytopathic effects, whereas Omicron produced rare, sporadic positive cells, with no apparent signs of epithelial injury (**Extended Data Fig. 8c**). Overall, these findings suggest that replication of Omicron in the mice respiratory tract is substantially attenuated compared to Omi-S, supporting our conclusion that mutations in S are only partially responsible for the attenuated pathogenicity of Omicron.

Mutations in S and nsp6 define Omicron attenuation

In addition to the S protein, Omicron has amino acid changes in non-structural protein 3 (nsp3), nsp4, nsp5, nsp6, nsp14, envelope (E), membrane (M), and N proteins, when compared with WT virus (**Extended Data Fig. 9a**). To identify non-spike protein(s) involved in Omicron attenuation, we generated a large panel of fluorescently labeled chimeric viruses, each containing Omicron S in combination with one non-spike protein of Omicron, while the remaining proteins were from WT virus (**Extended Data Fig. 9b**). Interestingly, when we combined Omicron S with Omicron nsp6 (Omi-S/nsp6), we observed a strong decrease in viral replication, with infection kinetics mimicking those of Omicron in cell culture (**Fig. 3a-d**); no such decrease was seen for other chimeric viruses. Poor replication efficiency of Omi-S/nsp6 was also corroborated by our finding that both Omi-S/nsp6 and Omicron took almost 5-6 days to recover by CPER, whereas all other variants were recovered in 2 days (data not shown). Finally, like Omicron, Omi-S/nsp6 was clearly outcompeted by Omi-S in a direct competition assay (**Fig. 3e**).

In lungs of K18-hACE2 mice, while Omi-S caused extensive bronchiolar infection and injury, both Omicron and Omi-S/nsp6 showed decreased infection with no evidence of epithelial damage (**Fig. 3f**). Consistent with these findings, lungs of Omi-S/nsp6-infected mice produced viral titers equivalent to those seen for rOmicron and Omicron isolate (**Fig. 3g**). Finally, 71% of mice infected with Omi-S/nsp6 survived (**Fig. 3h**), which contrasted with only 20% survival observed in mice infected with Omi-S (**Fig. 2c**). Overall, these results indicate that mutations in S and nsp6 are sufficient to define Omicron's attenuated pathogenicity. These observations support and further extend the findings of a recent study showing that mutations in the 5′UTR-nsp12 region, in which nsp6 resides, contribute to Omicron's attenuation in K18-hACE2 mice[31].

Spike RBM drives Omicron's vaccine escape

A large body of literature has demonstrated extensive escape of Omicron from vaccine-induced humoral immunity[14,19]. To define S regions associated with the immune escape phenotype of Omicron, we first compared the *in vitro* neutralization activity of sera from vaccinated individuals against WT SARS-CoV-2 (USA-WA1/2020), Omi-S, and Omicron. Sera collected within two months of the second dose of mRNA-1273 (Moderna mRNA vaccine; n = 12) or BNT162b2 (Pfizer-BioNTech mRNA vaccine; n = 12) vaccine were included (**Extended Data Table 1**). We performed a multicycle neutralization assay using a setting in which the virus and neutralizing sera were present at all times, mimicking the situation in a seropositive individual. All sera poorly neutralized Omicron, with 11.1-fold (range: 4.4- to 81.2-fold; $p < 0.0001$) lower half-maximal neutralizing dilution (ND_{50}) for Omicron compared with WA1 (**Fig. 4a,b**). In fact, around 80% of samples failed to completely neutralize Omicron at the highest tested concentration (**Extended Data Fig. 10**). Notably, Omi-S exhibited identical ND_{50} values to Omicron (11.5-fold lower than that of WA1; $p < 0.0001$) (**Fig. 4a,b**), suggesting that the Omicron S protein, when incorporated into a WT virus, behaves the same way as in Omicron.

The SARS-CoV-2 S protein comprises two domains: the S1 domain, which interacts with the ACE2 receptor, and the S2 domain, which is responsible for membrane fusion[33]. Within the S1 domain lie an N-terminal domain (NTD) and a receptor-binding domain (RBD), which harbors the receptor-binding motif (RBM) that makes direct contact with the ACE2 receptor[34]. The NTD of Omicron S carries 11 amino acid changes, including 6 deletions and one three-amino acid-long insertion, whereas the RBD harbors 15 mutations, 10 of which are concentrated in the RBM (**Extended Data Fig. 1**). Both NTD and RBD host neutralizing epitopes[35-38], but the RBD is immunodominant and represents the primary target of the neutralizing activity present in SARS-CoV-2 immune sera[38,39]. To determine if the neutralization resistance phenotype of Omicron is

caused by mutations in a particular S domain, we generated two groups of chimeric viruses. The first group comprised the WA1 virus carrying the NTD, RBD, or RBM of Omicron (**Fig. 4c**), and the second group consisted of Omi-S virus bearing the NTD, RBD, or RBM of WA1 (**Fig. 4d**). The neutralization assay showed that mutations in the RBM were the major cause of Omicron's resistance to vaccine-induced humoral immunity: replacing the RBM of WA1 with that of Omicron decreased ND_{50} by 5.4-fold ($p < 0.0001$), and conversely, substituting the RBM of Omi-S with that of WA1 increased ND_{50} by 5.6-fold ($p = 0.0003$) (**Fig. 4c,d**). The fact that none of the RBM-swap viruses achieved the difference of ~11-fold seen between WA1 and Omi-S suggests that mutations in other parts of S also contribute to vaccine resistance.

To investigate if specific mutations in Omicron RBM drive vaccine escape, we generated two additional panels of recombinant viruses, one with WA1 S carrying Omicron RBM mutations, either singly or in combination (**Fig. 4e**), and the other with Omicron S lacking the same set of mutations (**Fig. 4f**). Two WA1 mutants, mutant 3 (carrying E484A substitution) and mutant 4 (bearing a cluster of five substitutions Q493R, G496S, Q498R, N501Y, Y505H) exhibited a moderate but statistically significant decrease of 1.4-fold ($p = 0.0002$) and 1.8-fold ($p = 0.0003$) in ND_{50} values, respectively, compared with WA1 (**Fig. 4e**). The opposite was observed when these mutations were removed from Omicron S; the Omicron mutant 3 (lacking E484A substitution) and mutant 4 (lacking Q493R, G496S, Q498R, N501Y, Y505H) had a 1.9-fold ($p = 0.0082$) and 3.1-fold ($p = 0.0025$) higher ND_{50} values compared with Omicron (**Fig. 4f**). Since none of the mutants captured the overall phenotype of Omicron, we assume that the vaccine escape is a cumulative effect of mutations distributed along the length of the S protein. It is possible that mutations alter the conformation of Omicron S in such a manner that most of the immunodominant neutralizing epitopes are disrupted and become unavailable for neutralization.

DISCUSSION

This study provides important insights into viral proteins that contribute to SARS-CoV-2 pathogenicity. We show that S, the single most mutated protein in Omicron, has an incomplete role in Omicron attenuation. In cell-based infection assays, the Omi-S virus exhibits an intermediate replication efficiency between the ancestral virus and Omicron. Similarly, in K18-hACE2 mice, Omi-S contrasts with non-fatal Omicron and leads to 80% mortality; the ancestral virus causes 100% mortality in these animals. Importantly, when we combined S mutations with those in nsp6, the virus exhibited attenuated phenotype largely resembling that of Omicron, indicating that these two proteins are major determinants of Omicron pathogenicity. Future studies will decipher the mechanism(s) by which nsp6 mutations affect virus replication.

One potential limitation of our study is the use of K18-hACE2 mice for pathogenesis studies instead of the primate models that have more similarities with humans[40]. It should however be noted that K18-hACE2 mice are a well-established model for investigating the lethal phenotype of SARS-CoV-2[4,32]. While these mice develop lung pathology following SARS-CoV-2 infection, mortality has been associated with central nervous system involvement due to viral neuroinvasion and dissemination[32,41]. The fact that infection of K18-hACE2 mice with Omi-S, but not with Omicron, elicits neurologic signs (e.g., hunched posture and lack of responsiveness) suggests that the neuroinvasion property is preserved in Omi-S, probably due to its higher replication efficiency, and that the determinants of this property lie outside of the S protein. These findings are consistent with a recent hamster study showing that animals infected with Omi-S shed significantly more virus and lost more weight than those infected with Omicron, suggesting that mutations outside of S contribute to attenuated pathogenicity of Omicron[42].

We found that while the ancestral virus mainly replicates in lung alveoli and causes only rare infection of bronchioles in K18-hACE2 mice, both Omi-S and Omicron exhibit increased propensity to replicate in bronchiolar epithelium, indicating that the S protein is accountable for the changed tropism. The mechanism behind this switch is unknown, but it is possible that Omicron S is more efficient than WT S in utilizing Cathepsin B/L[25,43,44], which form an active viral entry pathway in bronchioles and other airway cells[45]. In contrast, SARS-CoV-2 entry into alveolar epithelial cells is mainly driven by TMPRSS2[28,46], which Omicron S is deficient in utilizing[25,47], leading to poor infection of these cells[4,25,30,44]. These findings may explain the attenuated lung pathology caused by Omicron.

Omicron nsp6 has two altered sites relative to the prototype SARS-CoV-2 Wuhan-Hu-1 isolate: a three-amino acid deletion (LSG, positions 105-107) and an I189V substitution (**Extended Data Fig. 9**). Several functions of nsp6 in coronavirus replication have been described, chief among them is the biogenesis of double membrane vesicles (DMVs), which represent the site of viral RNA synthesis[48-52]. A recent study showed that SARS-CoV-2 DMVs are mainly generated by concerted action of three viral proteins, nsp3, nsp4, and nsp6; while nsp3 and nsp4 are sufficient for formation of DMVs, nsp6 connects these DMVs with endoplasmic reticulum (ER) and channelizes the essential communication between these structures[48]. Whether the constellation of mutations in Omicron nsp6 affect the formation or functions of DMVs needs further investigation. Nsp6 also activates NLR3-dependent cytokine production and pyroptosis in the lungs of COVID-19 patients, serving as a key virulence factor[49]. Interestingly, nsp6 variant associated with asymptomatic COVID-19 exhibited a reduced ability to induce pyroptosis[49], prompting speculation that mutations in Omicron nsp6 may also influence pyroptosis. Detailed mechanistic studies will be required to dissect the effect of Omicron mutations on nsp6 functions.

It is currently unknown if mutations in S and nsp6 work in concert with each other to drive Omicron attenuation. Given that Omicron S showed higher predilection for bronchioles, it is possible that S is responsible for the altered viral tropism, whereas non-spike mutations, including those in nsp6, are mere adaptation to the changed tissue environment. It is worth mentioning that although nsp6 seems to be the major non-spike protein behind Omicron attenuation, the contribution of other viral proteins cannot be completely ruled out. *In vitro* experiments for the role of non-spike mutations were all carried out in ACE2/TMPRSS2/Caco-2 cells. Using other, more immune-competent, cell types may reveal the effect of other non-spike mutations as well. Further, our chimeric viruses contained Omicron S paired with only one non-spike protein at a time, which limited long-range epistatic interactions between mutations in multiple viral proteins.

Our study shows that mutations in the RBM of Omicron S are the major determinants of the viral escape from neutralizing antibodies, although mutations in other regions of S also contribute. Within the RBM, we identify two hotspots of mutations, which impart on Omicron S the ability to resist neutralization: one bearing the E484A substitution and the other harboring a cluster of five substitutions, Q493R, G496S, Q498R, N501Y and Y505H. The E484A substitution has been shown to escape neutralization by convalescent sera[53]. Further, structural modeling suggests that some therapeutic monoclonal antibodies establish highly stable salt bridges with the E484 residue, entirely losing their binding when this residue is changed to A or upon Q493K and Y505H changes[54]. Similarly, mapping of RBM residues that directly interact with 49 known neutralizing antibodies revealed N440, G446, S477, and T478 as low-frequently interactors, N501, Y505, and Q498 as medium-frequency interactors, and E484 and Q493 as high-frequency interactors[55], which is in line with our neutralization assay results. Interestingly, while antibody-binding potential of Omicron S is impaired[56], its receptor-binding capacity is intact. In fact, the

Omicron RBD has higher affinity for ACE2 relative to the Wuhan-Hu-1 and Delta RBDs[25]. This indicates that mutations in Omicron S have evolved in such a manner that they hinder antibody binding but preserve the receptor engagement. This opens up the possibility of targeting the conserved and structurally constrained regions of S involved in ACE2 recognition for the design of broad-spectrum vaccines to control the current COVID-19 pandemic.

MAIN REFERENCES

1 Liu, L. *et al.* Striking antibody evasion manifested by the Omicron variant of SARS-CoV-2. *Nature*, doi:10.1038/s41586-021-04388-0 (2021).

2 Planas, D. *et al.* Considerable escape of SARS-CoV-2 Omicron to antibody neutralization. *Nature*, doi:10.1038/s41586-021-04389-z (2021).

3 Schmidt, F. *et al.* Plasma Neutralization of the SARS-CoV-2 Omicron Variant. *N Engl J Med* **386**, 599-601, doi:10.1056/NEJMc2119641 (2022).

4 Shuai, H. *et al.* Attenuated replication and pathogenicity of SARS-CoV-2 B.1.1.529 Omicron. *Nature*, doi:10.1038/s41586-022-04442-5 (2022).

5 Halfmann, P. J. *et al.* SARS-CoV-2 Omicron virus causes attenuated disease in mice and hamsters. *Nature*, doi:10.1038/s41586-022-04441-6 (2022).

6 Lewnard, J. A. *et al.* Clinical outcomes associated with SARS-CoV-2 Omicron (B.1.1.529) variant and BA.1/BA.1.1 or BA.2 subvariant infection in Southern California. *Nat Med* **28**, 1933-1943, doi:10.1038/s41591-022-01887-z (2022).

7 Wolter, N. *et al.* Early assessment of the clinical severity of the SARS-CoV-2 omicron variant in South Africa: a data linkage study. *Lancet* **399**, 437-446, doi:10.1016/S0140-6736(22)00017-4 (2022).

8 Ulloa, A. C., Buchan, S. A., Daneman, N. & Brown, K. A. Estimates of SARS-CoV-2 Omicron Variant Severity in Ontario, Canada. *JAMA* **327**, 1286-1288, doi:10.1001/jama.2022.2274 (2022).

9 Uraki, R. *et al.* Characterization of SARS-CoV-2 Omicron BA.4 and BA.5 isolates in rodents. *Nature*, doi:10.1038/s41586-022-05482-7 (2022).

10 Uraki, R. *et al.* Characterization and antiviral susceptibility of SARS-CoV-2 Omicron BA.2. *Nature* **607**, 119-127, doi:10.1038/s41586-022-04856-1 (2022).

11 Dyer, O. Covid-19: Omicron is causing more infections but fewer hospital admissions than delta, South African data show. *BMJ* **375**, n3104, doi:10.1136/bmj.n3104 (2021).

12 Sigal, A. Milder disease with Omicron: is it the virus or the pre-existing immunity? *Nat Rev Immunol* **22**, 69-71, doi:10.1038/s41577-022-00678-4 (2022).

13 WHO. *Tracking SARS-CoV-2 variants*, <https://www.who.int/en/activities/tracking-SARS-CoV-2-variants/> (2022).

14 Cele, S. *et al.* Omicron extensively but incompletely escapes Pfizer BNT162b2 neutralization. *Nature* **602**, 654-656, doi:10.1038/s41586-021-04387-1 (2022).

15 Gu, H. *et al.* Probable Transmission of SARS-CoV-2 Omicron Variant in Quarantine Hotel, Hong Kong, China, November 2021. *Emerg Infect Dis* **28**, 460-462, doi:10.3201/eid2802.212422 (2022).
16 Iuliano, A. D. *et al.* Trends in Disease Severity and Health Care Utilization During the Early Omicron Variant Period Compared with Previous SARS-CoV-2 High Transmission Periods - United States, December 2020-January 2022. *MMWR Morb Mortal Wkly Rep* **71**, 146-152, doi:10.15585/mmwr.mm7104e4 (2022).
17 CDC. *COVID Data Tracker*, <https://covid.cdc.gov/covid-data-tracker/#variant-proportions> (2022).
18 Taylor, L. Covid-19: Omicron drives weekly record high in global infections. *BMJ* **376**, o66, doi:10.1136/bmj.o66 (2022).
19 Dejnirattisai, W. *et al.* SARS-CoV-2 Omicron-B.1.1.529 leads to widespread escape from neutralizing antibody responses. *Cell* **185**, 467-484 e415, doi:10.1016/j.cell.2021.12.046 (2022).
20 Suzuki, R. *et al.* Attenuated fusogenicity and pathogenicity of SARS-CoV-2 Omicron variant. *Nature*, doi:10.1038/s41586-022-04462-1 (2022).
21 Smyth, D. S. *et al.* Tracking cryptic SARS-CoV-2 lineages detected in NYC wastewater. *Nat Commun* **13**, 635, doi:10.1038/s41467-022-28246-3 (2022).
22 Kirby, A. E. *et al.* Notes from the Field: Early Evidence of the SARS-CoV-2 B.1.1.529 (Omicron) Variant in Community Wastewater - United States, November-December 2021. *MMWR Morb Mortal Wkly Rep* **71**, 103-105, doi:10.15585/mmwr.mm7103a5 (2022).
23 Herrmann, A. *et al.* Cloning of a Passage-Free SARS-CoV-2 Genome and Mutagenesis Using Red Recombination. *Int J Mol Sci* **22**, doi:10.3390/ijms221910188 (2021).
24 Liu, G. & Gack, M. U. An Optimized Circular Polymerase Extension Reaction-based Method for Functional Analysis of SARS-CoV-2. *BioRxiv*, doi:10.1101/2022.11.26.518005 (2022).
25 Meng, B. *et al.* Altered TMPRSS2 usage by SARS-CoV-2 Omicron impacts tropism and fusogenicity. *Nature*, doi:10.1038/s41586-022-04474-x (2022).
26 Willett, B. J. *et al.* SARS-CoV-2 Omicron is an immune escape variant with an altered cell entry pathway. *Nat Microbiol*, doi:10.1038/s41564-022-01143-7 (2022).
27 Martines, R. B. *et al.* Pathology and Pathogenesis of SARS-CoV-2 Associated with Fatal Coronavirus Disease, United States. *Emerg Infect Dis* **26**, 2005-2015, doi:10.3201/eid2609.202095 (2020).
28 Huang, J. *et al.* SARS-CoV-2 Infection of Pluripotent Stem Cell-Derived Human Lung Alveolar Type 2 Cells Elicits a Rapid Epithelial-Intrinsic Inflammatory Response. *Cell Stem Cell* **27**, 962-973 e967, doi:10.1016/j.stem.2020.09.013 (2020).
29 Mulay, A. *et al.* SARS-CoV-2 infection of primary human lung epithelium for COVID-19 modeling and drug discovery. *Cell Rep* **35**, 109055, doi:10.1016/j.celrep.2021.109055 (2021).
30 Halfmann, P. J. *et al.* SARS-CoV-2 Omicron virus causes attenuated disease in mice and hamsters. *Nature*, doi:10.1038/s41586-022-04441-6 (2022).
31 Liu, S., Selvaraj, P., Sangare, K., Luan, B. & Wang, T. T. Spike protein-independent attenuation of SARS-CoV-2 Omicron variant in laboratory mice. *Cell Rep* **40**, 111359, doi:10.1016/j.celrep.2022.111359 (2022).
32 Mariano Carossino, D. K., Aoife K. O'Connell, Paige Montanaro, Anna E. Tseng, Hans P. Gertje, Kyle A. Grosz, Maria Ericsson, Bertrand R. Huber, Susanna A. Kurnick, Saravanan

Subramaniam, Thomas A. Kirkland, Joel R. Walker, Kevin P. Francis, Alexander D. Klose, Neal Paragas, Markus Bosmann, Mohsan Saeed, Udeni B. R. Balasuriya, Florian Douam, Nicholas A. Crossland Fatal Neurodissemination and SARS-CoV-2 Tropism in K18-hACE2 Mice Is Only Partially Dependent on hACE2 Expression. *Viruses* **14** (2022).

33 Huang, Y., Yang, C., Xu, X. F., Xu, W. & Liu, S. W. Structural and functional properties of SARS-CoV-2 spike protein: potential antivirus drug development for COVID-19. *Acta Pharmacol Sin* **41**, 1141-1149, doi:10.1038/s41401-020-0485-4 (2020).

34 Lan, J. *et al.* Structure of the SARS-CoV-2 spike receptor-binding domain bound to the ACE2 receptor. *Nature* **581**, 215-220, doi:10.1038/s41586-020-2180-5 (2020).

35 Chi, X. *et al.* A neutralizing human antibody binds to the N-terminal domain of the Spike protein of SARS-CoV-2. *Science* **369**, 650-655, doi:10.1126/science.abc6952 (2020).

36 Voss, W. N. *et al.* Prevalent, protective, and convergent IgG recognition of SARS-CoV-2 non-RBD spike epitopes. *Science* **372**, 1108-1112, doi:10.1126/science.abg5268 (2021).

37 Premkumar, L. *et al.* The receptor binding domain of the viral spike protein is an immunodominant and highly specific target of antibodies in SARS-CoV-2 patients. *Sci Immunol* **5**, doi:10.1126/sciimmunol.abc8413 (2020).

38 Ju, B. *et al.* Human neutralizing antibodies elicited by SARS-CoV-2 infection. *Nature* **584**, 115-119, doi:10.1038/s41586-020-2380-z (2020).

39 Piccoli, L. *et al.* Mapping Neutralizing and Immunodominant Sites on the SARS-CoV-2 Spike Receptor-Binding Domain by Structure-Guided High-Resolution Serology. *Cell* **183**, 1024-1042 e1021, doi:10.1016/j.cell.2020.09.037 (2020).

40 Chang, M. C., Hild, S. & Grieder, F. Nonhuman primate models for SARS-CoV-2 research: Consider alternatives to macaques. *Lab Anim (NY)* **50**, 113-114, doi:10.1038/s41684-021-00755-6 (2021).

41 Kumari, P. *et al.* Neuroinvasion and Encephalitis Following Intranasal Inoculation of SARS-CoV-2 in K18-hACE2 Mice. *Viruses* **13**, doi:10.3390/v13010132 (2021).

42 Thomas P. Peacock, J. C. B., Jie Zhou, Nazia Thakur, Ksenia Sukhova, Joseph Newman, Ruthiran Kugathasan, Ada W.C. Yan, Wilhelm Furnon, Giuditta De Lorenzo, Vanessa M. Cowton, Dorothee Reuss, Maya Moshe, Jessica L. Quantrill, Olivia K. Platt, Myrsini Kaforou, Arvind H. Patel, Massimo Palmarini, Dalan Bailey, and Wendy S. Barclay. The altered entry pathway and antigenic distance of the SARS-CoV-2 Omicron variant map to separate domains of spike protein. *bioRxiv*, doi:10.1101/2021.12.31.474653 (2022).

43 Pranesh Padmanabhan, N. M. D. Evidence of increased Cathepsin B/L and decreased TMPRSS2 usage for cell entry by the SARS-CoV-2 Omicron variant. *bioRxiv*, doi:10.1101/2022.01.13.476267 (2022).

44 Hui, K. P. Y. *et al.* SARS-CoV-2 Omicron variant replication in human bronchus and lung ex vivo. *Nature*, doi:10.1038/s41586-022-04479-6 (2022).

45 Thomas P. Peacock, J. C. B., Jie Zhou, Nazia Thakur, Joseph Newman, Ruthiran Kugathasan, Ksenia Sukhova, Myrsini Kaforou, Dalan Bailey, Wendy S. Barclay. The SARS-CoV-2 variant, Omicron, shows rapid replication in human primary nasal epithelial cultures and efficiently uses the endosomal route of entry. *bioRxiv*, doi:10.1101/2021.12.31.474653 (2022).

46 Grau-Exposito, J. *et al.* Evaluation of SARS-CoV-2 entry, inflammation and new therapeutics in human lung tissue cells. *PLoS Pathog* **18**, e1010171, doi:10.1371/journal.ppat.1010171 (2022).

47 Zhao, H. *et al.* SARS-CoV-2 Omicron variant shows less efficient replication and fusion activity when compared with Delta variant in TMPRSS2-expressed cells. *Emerg Microbes Infect* **11**, 277-283, doi:10.1080/22221751.2021.2023329 (2022).
48 Ricciardi, S. *et al.* The role of NSP6 in the biogenesis of the SARS-CoV-2 replication organelle. *Nature* **606**, 761-768, doi:10.1038/s41586-022-04835-6 (2022).
49 Sun, X. *et al.* SARS-CoV-2 non-structural protein 6 triggers NLRP3-dependent pyroptosis by targeting ATP6AP1. *Cell Death Differ* **29**, 1240-1254, doi:10.1038/s41418-021-00916-7 (2022).
50 Cottam, E. M., Whelband, M. C. & Wileman, T. Coronavirus NSP6 restricts autophagosome expansion. *Autophagy* **10**, 1426-1441, doi:10.4161/auto.29309 (2014).
51 Benvenuto, D. *et al.* Evolutionary analysis of SARS-CoV-2: how mutation of Non-Structural Protein 6 (NSP6) could affect viral autophagy. *J Infect* **81**, e24-e27, doi:10.1016/j.jinf.2020.03.058 (2020).
52 Gosert, R., Kanjanahaluethai, A., Egger, D., Bienz, K. & Baker, S. C. RNA replication of mouse hepatitis virus takes place at double-membrane vesicles. *J Virol* **76**, 3697-3708, doi:10.1128/jvi.76.8.3697-3708.2002 (2002).
53 Liu, Z. *et al.* Identification of SARS-CoV-2 spike mutations that attenuate monoclonal and serum antibody neutralization. *Cell Host Microbe* **29**, 477-488 e474, doi:10.1016/j.chom.2021.01.014 (2021).
54 Shah, M. & Woo, H. G. Omicron: A Heavily Mutated SARS-CoV-2 Variant Exhibits Stronger Binding to ACE2 and Potently Escapes Approved COVID-19 Therapeutic Antibodies. *Front Immunol* **12**, 830527, doi:10.3389/fimmu.2021.830527 (2021).
55 Ye, G., Liu, B. & Li, F. Cryo-EM structure of a SARS-CoV-2 omicron spike protein ectodomain. *Nat Commun* **13**, 1214, doi:10.1038/s41467-022-28882-9 (2022).
56 Carreno, J. M. *et al.* Activity of convalescent and vaccine serum against SARS-CoV-2 Omicron. *Nature* **602**, 682-688, doi:10.1038/s41586-022-04399-5 (2022).

FIGURE LEGENDS

Fig. 1: Effect of spike on *in vitro* growth kinetics of Omicron. a, Schematic of viruses. S, spike; N, nucleocapsid. **b-e,** ACE2/TMPRSS2/Caco-2 and Vero E6 cells were infected at an MOI of 0.01, and the percentage of nucleocapsid (N)-positive cells (n = 6 replicates) (**b,c**) and the release of infectious particles (n = 3 replicates) (**d,e**) were determined by flow cytometry and the plaque assay, respectively. **f,** ACE2/TMPRSS2/Caco-2 were infected with virus mixtures at a 1:1 ratio to obtain the final MOI of 0.005 for each virus. The cells were fixed at indicated times and subjected to flow cytometry. Left. Representative dot plot; right, fraction of uninfected, Omi-S/mCherry-infected, Omicron/mNeoGreen-infected, and doubly infected cells. Singly infected

cells were used for compensation. Error bars, mean ± SD (n = 3 replicates). **g,** Plaque sizes. Left, representative images of plaques on ACE2/TMPRSS2/Caco-2 cells. Right, diameter of plaques is plotted as mean ± SD of 20 plaques per virus. **h,** Human induced pluripotent stem cell-derived alveolar type 2 epithelial cells were infected at an MOI of 2.5 for 48h or 96h. The apical side of cells was washed with 1X PBS and the levels of infectious virus particle were measured by the plaque assay. Error bars, mean ± SD (n = 4 replicates). Experiments were repeated twice, with each experimental repeat containing 3 (**b-g**) or 4 (**h**) replicates. *p* values were calculated by a two-tailed, unpaired *t*-test with Welch's correction. *p <0.05, **p <0.01, ***p <0.001, and ****p < 0.0001; ns, not significant. The gating strategy for flow cytometry is shown in Supplementary Fig. 1.

Fig. 2: Role of spike in Omicron pathogenicity. a-c, Male and female K18-hACE2 mice (aged 12-20 weeks) were intranasally inoculated with 1 x 10^4 PFU of WT (n = 6 mice), Omi-S (n = 10 mice), or Omicron (n = 10 mice). Two independently generated virus stocks were used in this experiment. The body weight (**a**), clinical score (**b**), and survival (**c**) were monitored daily for 14 days. Animals losing 20% of their initial body weight were euthanized. **d,e,** K18-hACE2 mice were intranasally inoculated with 1 x 10^4 PFU of WT (n = 14 mice), Omi-S (n = 14 mice), and Omicron (n = 14 mice). Lung samples of the infected mice were collected at 2 or 4 dpi to determine the viral titer (n = 4 mice) (**d**) or for immunohistochemistry (IHC) detection of the N protein (n = 3 mice) (**e**). In e, representative IHC images showing SARS-CoV-2 N (brown color) in alveoli (arrows) and bronchioles (arrowheads) in mice lungs at 2 dpi are presented. (Scale bar = 100 μm). **f,** The percentage of N-positive bronchioles in the lungs of infected mice (n = 3 mice). Each dot represents an infected animal. Statistical significance was determined using two-tailed, unpaired

t-test with Welch's correction (**a,b,d,f**) and log-rank (Mantel-Cox) test (**c**). **p* <0.05, ***p* <0.01, ****p* <0.001, and *****p* < 0.0001; ns, not significant.

Fig. 3: Mutations in spike and nsp6 drive Omicron pathogenicity. a-d, Replication kinetics of indicated mNeonGreen reporter viruses in ACE2/TMPRSS2/Caco-2 cells (MOI=0.01) determined by flow cytometry (n = 3 replicates) (**a,c**) and plaque assay (n = 3 replicates) (**b,d**). Experiments were repeated twice. **e,** ACE2/TMPRSS2/Caco-2 cells were infected with virus mixtures at 1:1 ratio to obtain the final MOI of 0.005 for each virus. The cells were fixed at indicated times and analyzed by flow cytometry. Fraction of uninfected, singly infected, and doubly infected cells is shown. Singly infected cells were used for compensation. Individual data points are plotted along with the mean ± SD (n = 3 replicates). The experiment was repeated twice. **f-h,** K18-hACE2 mice were intranasally inoculated with 1 x 10^4 PFU of viruses. Lung samples of infected mice were collected at 2 dpi for immunohistochemistry (IHC) detection of the N protein (n = 3 mice) (**f**) or for determination of viral titers (n = 4 mice) (**g**). In f, representative images of hematoxylin and eosin (H&E) staining of N-positive bronchioles are shown in insets. Bronchiolar epithelial necrosis is indicated with arrows. No evidence of necrosis was seen in bronchioles of mice infected with Omicron or Omi-S/nsp6. (Scale bar = 100 μm). The right panel in f shows the percentage of N-positive bronchioles in the lungs of infected mice. Each dot represents an infected animal. **h,** Survival of infected animals monitored daily for 14 days. Animals losing 20% of their initial body weight were euthanized. Statistical significance was determined using two-tailed, unpaired *t*-test with Welch's correction (**a-g**) and log-rank (Mantel-Cox) test (**h**). **p* <0.05, ***p* <0.01, ****p* <0.001, and *****p* < 0.0001; ns, not significant.

Fig. 4: Role of spike in immune resistance of Omicron. a, ND_{50} values for WA1, Omi-S, and Omicron in sera from individuals who received two shots of Moderna (donor 1-12) or Pfizer (donor

13-24) vaccine (further details of sera are provided in Extended Data Table 1; individual curves are shown in Extended Data Fig. 10). **b,** Trajectories of ND_{50} values against WA1, Omi-S, and Omicron (the data from a is plotted). Fold-change in ND_{50} values is indicated (n = 24 serum samples). **c,d,e,f,** Schematic of the chimeric (**left panels; c,d**) and mutant (**left panels; e,f**) viruses. The amino acid numbering for WA1 mutants in e is based on the WA1 S sequence, whereas the numbering for Omicron mutants in f is based on the Omicron S sequence. Six of the 24 sera (three from Moderna and three from Pfizer) were tested. Each serum sample is represented by a dot of specific color. The data are plotted as fold-change of the parental virus. **p* <0.05, ***p* <0.01, ****p* <0.001, and *****p* < 0.0001; ns, not significant; two-tailed, unpaired *t* test with Welch's correction.

METHODS

Cells, antibodies, and plasmids

The cell lines were incubated at 37ºC and 5% CO_2 in a humidified incubator. Human embryonic kidney HEK293T cells (ATCC; CRL-3216), human lung adenocarcinoma A549 cells (ATCC; CCL-185), human colorectal adenocarcinoma Caco-2 cells (ATCC; HTB-37), and African green monkey kidney Vero E6 cells were maintained in DMEM (Gibco; #11995-065) containing 10% FBS and 1X non-essential amino acids. Lentiviral delivery system was used to generate cells stably expressing human ACE2 and TMPRSS2. Mycoplasma negative status of all cell lines was confirmed.

Anti-SARS-CoV nucleocapsid (N) protein antibody (Rockland; #200-401-A50; 1:2000) was used to detect the SARS-CoV-2 N protein by IF and western blot. Mouse anti-SARS-CoV-2 spike

antibody (GeneTex; #GTX632604; 1:1000), directed against the S2 subunit, was used for western blot analysis of spike cleavage in virus particles and infected cells.

Plasmids encoding various fragments of the SARS-CoV-2 genome (Hu/DP/Kng/19-020 isolate) were a generous gift from Yoshiharu Matsuura[57]. We replaced the spike gene in the plasmid pCSII-SARS-CoV-2 F8[57] with the chemically synthesized Omicron spike gene and named this plasmid pCSII-SARS-CoV-2 F8_Omicron. We replaced the open reading frame (ORF) 7 in the plasmid pcDNA3.1-SARS-CoV-2 F9+10 with mNeonGreen or mCherry to obtain plasmids pcDNA3.1-SARS-CoV-2 F9+10_mNG and pcDNA3.1-SARS-CoV-2 F9+10_mCherry, respectively. The plasmids pMW-CoV-2-UTRlinker[57] and pGL-CPERlinker[24], both containing a linker fragment comprising hepatitis delta virus ribozyme (HDVr), the bovine growth hormone polyadenylation signal sequence (BGH-polyA), and cytomegalovirus (CMV) promoter have been previously reported. The lentiviral vectors, pLOC_hACE2_PuroR and pLOC_hTMPRSS2_BlastR, containing human ACE2 and TMPRSS2, respectively, have been described previously[58].

Biocontainment

All procedures were performed in a state-of-the-art biosafety level 3 (BSL3) facility at the National Emerging Infectious Diseases Laboratories (NEIDL) of Boston University using biosafety protocols approved by the Institutional Biosafety Committee (IBC). The experimental plans, including the generation of recombinant chimeric viruses, were reviewed and approved by the IBC, which comprises scientists, biosafety and compliance experts as well as local community members. Furthermore, the research was approved by the Boston Public Health Commission. All personnel received rigorous biosafety, biosecurity, and BSL3 training before participating in experiments. Special personal protective equipment, including scrubs, disposable overalls, shoe covers, double-layered gloves, and powered air-purifying respirators were used. Biosecurity

measures are built in the environment through building and security systems and are reinforced through required training programs, standing meetings, and emergency exercises. The researchers involved in working with chimeric viruses received at least two booster shots of the SARS-CoV-2 mRNA vaccine before the study was started. Finally, all researchers were medically cleared by the Boston University Research Occupational Health Program.

Collection of serum samples

Sera from individuals who received two doses of mRNA-1273 (Moderna) or BNT162b2 (Pfizer) vaccine were collected at Boston Medical Center at least two weeks after the final dose. These individuals had no prior history of SARS-CoV-2 infection. Serum samples were collected using protocols reviewed and approved by the Institutional Review Board at Boston Medical Center. All methods were performed in accordance with relevant guidelines and regulations. The participants provided electronic informed consent. De-identified samples were used in this research. Additional information for serum samples is provided in Extended Data Table 1.

Omicron stock preparation and titration

The SARS-CoV-2 BA.1 Omicron virus stock was generated in ACE2/TMPRSS2/Caco-2 cells. Briefly, 5 x 10^5 cells, grown overnight in DMEM/10%FBS/1X NEAA in one well of a 6-well plate, were inoculated with the collection medium in which the nasal swab from a SARS-CoV-2 patient was immersed. The swab material was obtained from the Department of Public Health, Massachusetts, and it contained the sequence-verified Omicron virus (NCBI accession number: OL719310). Twenty-four hours after infecting cells, the culture medium was replaced with 2 ml of DMEM/2%FBS/1X NEAA and the cells were incubated for another 72h, at which point the CPE became visible. The culture medium was harvested, passed through a 0.45 μ filter, and kept at -

80ºC as a P0 virus stock. To generate a P1 stock, we infected 1 x 10^7 ACE2/TMPRSS2/Caco-2 cells, seeded the day before in a T175 flask, with the P0 virus at an MOI of 0.01. The next day, the culture medium was changed to 25 ml of 2% FBS-containing medium. Three days later, when the cells exhibited excessive CPE, the culture medium was harvested, passed through a 0.45 μ filter, and stored at -80ºC as a P1 stock.

To titrate the virus stock, we seeded ACE2/TMPRSS2/Caco-2 cells into a 12-well plate at a density of 2 x 10^5 cells per well. The next day, the cells were incubated with serial 10-fold dilutions of the virus stock (250 μl volume per well) for 1h at 37ºC, overlayed with 1 ml per well of medium containing 1:1 mixture of 2X DMEM/4% FBS and 1.2% Avicel (DuPont; RC-581), and incubated at 37ºC for another three days. To visualize the plaques, the cell monolayer was fixed with 4% paraformaldehyde and stained with 0.1% crystal violet, with both fixation and staining performed at room temperature for 30 minutes each. The number of plaques were counted and the virus titer was calculated.

Recombinant SARS-CoV-2 generation by CPER

SARS-CoV-2 recombinant viruses were generated by using a recently described optimized CPER protocol[24]. Full-length SARS-CoV-2 cDNA cloned into a bacterial artificial chromosome (BAC)[23] was employed to generate WT and Omi-S viruses. Briefly, the BAC was amplified into eight overlapping fragments (F1, F2, F3, F4, F5, F6, F7, and F9) covering the whole SARS-CoV-2 genome. The pCSII-SARS-CoV-2 F8 (containing a D614G substitution) and pCSII-SARS-CoV-2 F8_Omicron plasmids, which were used to generate S mutants, served as templates for amplification of fragment 8 (F8). The UTR linker plasmids pMW-CoV-2-UTRlinker[57] or pGL-CPERlinker[24] were used as a template to amplify the linker sequence. The 5' termini of all ten DNA fragments (F1-F9 and the linker) were phosphorylated by using T4 PNK (NEB; #M0201).

The CPER reaction containing equimolar amounts (0.05 pmol) of each fragment was carried out with PrimeStar GXL DNA polymerase (Takara Bio; #R050A) as previously described[24]. The nicks in the circular product were sealed by using HiFi Taq DNA ligase (NEB; #M0647S).

To generate chimeric viruses containing a combination of Omicron S and non-spike proteins (Omi-S/nsp3, Omi-S/nsp4, Omi-S/nsp5, Omi-S/nsp6, Omi-S/nsp14, Omi-S/E, Omi-S/M, and Omi-S/N), we used SARS-CoV-2 plasmids described in Torii S et al. as templates, generously provided by Dr. Yoshiharu Matsuura[57]. These plasmids contained SARS-CoV-2 sequences derived from the SARS-CoV-2/Hu/DP/Kng/19-020 strain. We introduced mutations into these plasmids using the standard DNA recombination technology. Our chimeric viruses also contained P323L substitution in nsp12. Plasmid sequences were confirmed by Sanger method.

To transfect cells with the CPER product, we seeded ACE2/TMPRSS2/Caco-2 cells into a 6-well plate at a density of 5 x10^5 cells per well. The transfection mix was prepared by mixing 26 µl of the original 52 µl CPER reaction volume with 250 µl of Opti-MEM (Thermo Fisher Scientific; #31985070) and 6 µl of TransIT-X2 Dynamic Delivery System (Mirus Bio; #MIR 6000). Following incubation at room temperature for 25 min, the transfection mix was added to the cells. The next day, the culture medium was replaced with fresh DMEM containing 2% FBS. The CPE became visible in 3-4 days, at which point the culture medium was collected and stored as a P0 virus stock. The P0 stock was used for experiments described in this manuscript. The sequence of CPER-generated viruses was confirmed by next generation sequencing.

SARS-CoV-2 whole viral sequencing and genome assembly

cDNA synthesis was performed using Superscript IV reverse transcriptase (Invitrogen, Waltham, MA, USA). Whole viral amplification was performed using NEB Varskip protocol using multiplexed primer pools designed with Primal Scheme generating 400-bp tiling amplicons. PCR

products from the Varskip protocol were pooled together and Illumina library construction was performed using the Nextera XT Library Prep Kit (Illumina, San Diego, CA, USA). Deep sequencing data analysis was carried out using the Stanford Coronavirus Antiviral & Resistance Database (CoV-RDB) platform[59]. Input FASTQ sequence alignment with Wuhan-Hu-1 reference was done using MiniMap2 version 2.22 in CodFreq pipeline (https://github.com/hivdb/codfreq). The output of MiniMap2, an aligned SAM file, was converted to a CodFreq file by an in-house written Python script using a PySam library (version: 0.18.0) and further analyzed with the CoVDB. SARS-COV-2 variant calling was done using CoVDB Scorpio call v.1.2.123 (https://pangolin.cog-uk.io/)[60] and Nextclade v.1.13.2 (https://clades.nextstrain.org/)[61]. PCR and sequencing run were performed once with the appropriate positive and negative controls.

SARS-CoV-2 neutralization assay

For neutralization assays, initial 1:10 dilutions of plasma, obtained from individuals who received two shots of either Moderna or Pfizer mRNA-based SARS-CoV-2 vaccine, were five-fold serial diluted in Opti-MEM over seven or eight dilutions. These plasma dilutions were then mixed at a 1:1 ratio with 1.25 x 10^4 infectious units of SARS-CoV-2 and incubated for 1h at 37ºC. Thereafter, 100 µl of this mixture was directly applied to ACE2/A549 cells seeded the previous day in poly-L-lysine-coated 96-well plates at a density of 2.5 x 10^4 cells per well in 100 µl volume. Thus, the final starting dilution of plasma was 1:20 and the final MOI was 0.5. The cells were incubated at 37ºC for 24h, after which they were fixed and stained with an anti-nucleocapsid antibody. When PBS instead of plasma was used as a negative control, these infection conditions resulted in around 40-50% infected cells at 24 hpi.

Generation and infection of iAT2 cells

The detailed protocol for generation of human iPSC-derived alveolar epithelial type II cells (iAT2s) has been published in our recent papers[28,62]. The air-liquid interface (ALI) cultures were established by preparing single cell suspensions of iAT2 3D sphere cultures grown in Matrigel. Briefly, Matrigel droplets containing iAT2 spheres were dissolved in 2 mg/ml dispase (Sigma) and the spheres were dissociated in 0.05% trypsin (GIBCO) to generate a single-cell suspension. 6.5 mm Transwell inserts (Corning) were coated with dilute Matrigel (Corning) in accordance with the manufacturer's protocol. Single-cell iAT2s were plated on Transwells at a density of 520,000 cells/cm2 in 100 µl of CK+DCI medium containing 10 µM of rho-associated kinase inhibitor ("Y"; Sigma Y-27632). 600 µl of this medium was added to the basolateral compartment. 24h after plating, the basolateral medium was changed with fresh CK+DCI+Y medium. 48h after plating, the apical medium was aspirated to initiate ALI culture. 72h after plating, basolateral medium was replaced with CK+DCI medium to remove the rho-associated kinase inhibitor. Basolateral medium was changed every two days thereafter. The detailed composition of CK+DCI medium is provided in our previous publications[28,62].

iAT2 cells in ALI cultures were infected with purified SARS-CoV-2 stock at an MOI of 2.5 based on the titration done on ACE2/TMPRSS2/Caco-2 cells. For infection, 100 µl of inoculum prepared in 1X PBS (or mock-infected with PBS-only) was added to the apical chamber of each Transwell and incubated for 2h at 37ºC followed by the removal of the inoculum and washing of the apical side three times with 1X PBS (100 µl/wash). The cells were incubated for two or four days, after which the newly released virus particles on the apical side were collected by adding 100 µl of 1X PBS twice to the apical chamber and incubating at 37ºC for 15 min. The number of infectious virus particles in the apical washes were measured by the plaque assay on ACE2/TMPRSS2/Caco-2 cells. For flow cytometry, iAT2 cells were detached by adding 0.2 ml

Accutase (Sigma; #A6964) apically and incubated at room temperature for 15 min. The detached cells were pelleted by low-speed centrifugation, fixed in 10% formalin, and stained with anti-SARS-CoV-2 N antibody.

Detection of spike incorporation and cleavage in SARS-CoV-2 particles

The culture medium of ACE2/TMPRSS2/Caco-2 cells transfected with the CPER product was collected and passed through 0.22 μm filters. The SARS-CoV-2 particles were pelleted down by mixing an equal volume of the culture medium with 20% PEG6000 in PBS followed by overnight incubation at 4ºC. The mixture was centrifuged at 12,000*g* for 30 min at 4ºC, and the pellet was resuspended in 1X SDS sample buffer. The protein concentration was measured by the BCA assay using Pierce BCA Protein Assay kit (ThermoFisher Scientific; #23225). Equal amounts of protein were resolved on 4-12% SDS page. Spike was detected with mouse anti-SARS-CoV-2 spike antibody (GeneTex; #GTX632604; 1:1000) and IRDye 800CW donkey anti-mouse IgG secondary antibody (LI-COR Biosciences; #926-32212; 1:5000). The bands were visualized by scanning the membrane with the LiCor CLx infrared scanner. The open-source package, ImageJ (version 1.53a), was used to measure the intensity of protein bands.

Flow cytometry

For flow cytometry, fixed cells were permeabilized in 1x permeabilization buffer (ThermoFisher Scientific; #00-5523-00) and stained with SARS-CoV-2 nucleocapsid antibody (Rockland; #200-401-A50, 1:1,000), followed by donkey anti-rabbit IgG-AF647 secondary antibody (ThermoFisher Scientific; #A-31573). Cells infected with fluorescent reporter viruses were fixed and analyzed without staining. Gating was based on uninfected, stained control cells. The extent of staining was quantified using a BD LSR II flow cytometer (BD Biosciences, CA),

and the data were analyzed with FlowJo v10.6.2 (FlowJo, Tree Star Inc). The gating strategy for flow cytometry is shown in Supplementary Fig. 1.

Immunofluorescence

Immunofluorescence was performed as described in our previous publication[58]. Briefly, virus-infected cells were fixed in 4% paraformaldehyde and permeabilized in a buffer containing 0.1% Triton X-100 prepared in PBS. Following blocking in a buffer containing 0.1% Triton X-100, 10% goat serum, and 1% BSA, the cells were incubated overnight at 4ºC with anti-SARS-CoV Nucleocapsid antibody (1:2,000 dilution). The cells were then stained with Alexa Fluor 568-conjugated goat anti-rabbit secondary antibody (1:1000 dilution) (Invitrogen; #A11008) in the dark at room temperature for 1h and counterstained with DAPI. Images were captured using the ImageXpress Micro Confocal (IXM-C) High-Content Imaging system (Molecular Devices) with a 4x S Fluor objective lens at a resolution of 1.7 micron/pixel in the DAPI (excitation: 400 nm/40 nm, emission: 447 nm/60 nm) and TexasRed (excitation: 570nm/80nm, emission: 624nm/40nm) channels. Both channels were used to establish their respective laser autofocus offsets. The images were analyzed using MetaXpress High Content Image Acquisition and Analysis software (Molecular Devices). First, the images were segmented using the CellScoring module. The objects between 7 and 20 microns in diameter and greater than 1800 gray level units in intensity were identified and classified as nuclei. Positive cells were taken as nuclei having TexasRed signal of 1500 gray level units or above within 10 to 20 microns of each nucleus. The remaining objects were set to negative cells. From these objects, the following readouts were measured and used for downstream analysis: Total number of positive and negative cells, total area of positive cells, and integrated intensity in the TexasRed channel for positive cells. To calculate the 50%

neutralizing dilution (ND_{50}), we performed a non-linear regression curve fit analysis using Prism 9 software (GraphPad).

Mice maintenance and approvals

Mice were maintained in a facility accredited by the Association for the Assessment and Accreditation of Laboratory Animal Care (AAALAC). Animal studies were performed following the recommendations in the Guide for the Care and Use of Laboratory Animals of the National Institutes of Health. The protocols were approved by the Boston University Institutional Animal Care and Use Committee (IACUC). Heterozygous K18-hACE2 C57BL/6J mice (Strain 2B6.Cg-Tg(K18-ACE2)2Prlmn/J) were purchased from the Jackson Laboratory (Jax, Bar Harbor, ME). Animals were housed in groups of 4-5 in ventilated cages (Tecniplast, Buguggiate, Italy) and maintained on a 12:12 light cycle at 30-70% humidity, 68F temperature, ad libitum water, and ad libitum standard chow diet (LabDiet, St. Louis, MO).

Mice infection

Male and female K18-hACE2 mice (12-20 weeks old) were inoculated intranasally with 10^4 PFU of SARS-CoV-2 in 50 µl of sterile 1X PBS. The inoculations were performed under 1-3% isoflurane anesthesia. *In vivo* experiments were not blinded, and animals were randomly assigned to infection groups. No a priori sample size calculation was performed. Instead, samples sizes were determined based on our previous animal work. 26 mice (6 for WT, 10 for Omi-S, and 10 for Omicron) were enrolled in a 14-day survival study, and another 42 mice (14 for each of the WT, Omi-S, and Omicron viruses) were used for virological and histological analysis of infected lungs. During the survival study, the animals were monitored for body weight, respiration, general appearance, responsiveness, and neurologic signs. An IACUC-approved clinical scoring system

751 was used to monitor disease progression and define humane endpoints. The score of 1 was given
752 for each of the following situations: body weight, 10-19% loss; respiration, rapid and shallow with
753 increased effort; appearance, ruffled fur and/or hunched posture; responsiveness, low to
754 moderate unresponsiveness; and neurologic signs, tremors. The sum of these individual scores
755 constituted the final clinical score. Animals were considered moribund and humanly euthanized
756 in case of weight loss greater than or equal to 20%, or if they received a clinical score of 4 or
757 above for two consecutive days. Body weight and clinical score were recorded once per day for
758 the duration of the study. For the purpose of survival curves, animals euthanized on a given day
759 were counted dead the day after. Animals found dead in cage were counted dead on the same
760 day. For euthanization, an overdose of ketamine was administered followed by a secondary
761 method of euthanization.

762 For quantification of SARS-CoV-2 infectious particles in lungs by the plaque assay, lung
763 tissues were collected in 600 µl of RNAlater stabilization solution (ThermoFisher Scientific;
764 #AM7021) and stored at -80ºC until analysis. 20-40 mg of tissue was placed in a tube containing
765 600 µl of OptiMEM and a 5 mm stainless steel bead (Qiagen; #69989) and homogenized in the
766 Qiagen TissueLyser II by two dissociation cycles (1,800 oscillations/minute for 2 minutes) with a
767 one-minute interval between cycles. The homogenate was centrifuged at 15,000*g* for 10 minutes
768 at room temperature and the supernatant was transferred to a new tube. Ten-fold serial dilutions
769 of this supernatant were used for the plaque assay on ACE2/TMPRSS2/Caco-2 cells, as
770 described above.

771 For IHC and histologic analysis, the insufflated whole lung tissues were inactivated in 10%
772 neutral buffered formalin at a 20:1 fixative to tissue ratio for a minimum of 72h before removal

from BSL3 in accordance with an approved IBC protocol. Tissues were subsequently processed, embedded in paraffin and five-micron sections stained with hematoxylin and eosin (H&E) following standard histological procedures. IHC was performed using a Ventana BenchMark Discovery Ultra autostainer (Roche Diagnostics, USA). An anti-SARS-CoV-2 S antibody (Cell Signaling technologies: clone E5S3V) or anti-SARS-CoV-2 N antibody (Cell Signaling technologies: clone 1C7C7) that showed equivalent immunoreactivity against WT and Omicron proteins was used to identify virus-infected cells. For the SARS-CoV-2 N antibody, given its mouse origin, an additional rabbit anti-mouse anti-Ig1 + Ig2a + IgG3 antibody (Abcam; #133469) was used to prevent non-specific binding. A HRP conjugated goat anti-rabbit IgG polymer detection was then used to detect the viral specific antibodies (Vector Laboratories, USA: MP-7451) and finally developed using 3, 3'-Diaminobenzidine (DAB) chromogen and counterstained with hematoxylin. Negative and positive controls for IHC included blocks of uninfected and SARS-CoV-2-infected Vero E6 cells, respectively.

For quantification of N protein in the nasal turbinate epithelium, digitalized whole slide scans were analyzed using the image analysis software HALO (Indica Labs, Inc., Corrales, NM, USA). The respiratory epithelium was manually annotated to create a layer for downstream analysis. Area quantification (AQ) was performed to determine percentages of SARS-CoV-2 Nucleoprotein in the annotated layer, which generated percentage of immunoreactivity output.

DATA AVAILABILITY

All data supporting the conclusions of this study are reported in the paper. The raw data are available from the corresponding author with no restrictions upon reasonable request.

CODE AVAILABILITY

No code was used for data acquisition in this study.

ADDITIONAL REFERENCES

57 Torii, S. *et al.* Establishment of a reverse genetics system for SARS-CoV-2 using circular polymerase extension reaction. *Cell Rep* **35**, 109014, doi:10.1016/j.celrep.2021.109014 (2021).

58 Chen, D. Y. *et al.* SARS-CoV-2 Disrupts Proximal Elements in the JAK-STAT Pathway. *J Virol* **95**, e0086221, doi:10.1128/JVI.00862-21 (2021).

59 Tzou, P. L., Tao, K., Pond, S. L. K. & Shafer, R. W. Coronavirus Resistance Database (CoV-RDB): SARS-CoV-2 susceptibility to monoclonal antibodies, convalescent plasma, and plasma from vaccinated persons. *PLoS One* **17**, e0261045, doi:10.1371/journal.pone.0261045 (2022).

60 Rambaut, A. *et al.* A dynamic nomenclature proposal for SARS-CoV-2 lineages to assist genomic epidemiology. *Nat Microbiol* **5**, 1403-1407, doi:10.1038/s41564-020-0770-5 (2020).

61 Aksamentov I, R. C., Hodcroft E, Neher R. Nextclade: clade assignment, mutation calling and quality control for viral genomes. *Journal of Open Source Software*, doi:10.21105/joss.03773 (2021).

62 Jacob, A. *et al.* Derivation of self-renewing lung alveolar epithelial type II cells from human pluripotent stem cells. *Nat Protoc* **14**, 3303-3332, doi:10.1038/s41596-019-0220-0 (2019).

ACKNOWLEDGEMENT

We thank Dr. Yoshiharu Matsuura from Osaka University, Japan, for providing plasmids carrying fragments of the SARS-CoV-2 genome and the linker plasmid pMW-CoV-2-UTRlinker; the Department of Public Health, Massachusetts, for providing the clinical specimen containing Omicron virus; and the ICCB-Longwood Screening Facility of Harvard Medical School for assistance with IF image acquisition and analysis. This work was supported by Boston University startup funds (to MS and FD); NIH S10 Shared Instrumentation Grants, S10-OD026983 and SS10-OD030269 (to NAC); Peter Paul Career Development Award (to FD); and BMBF SenseCoV2 01KI20172A, DFG Fokus COVID-19, EN 423/7-1, and coronavirus research grants by the Bavarian State Ministry of Science and the Arts and Bavarian State Ministry of Health Bay-VOC (to AE). We thank the Evans Center for Interdisciplinary Biomedical Research at Boston

University School of Medicine for their support of the Affinity Research Collaborative on 'Respiratory Viruses: A Focus on COVID-19'.

AUTHOR CONTRIBUTIONS

M.S. conceptualized the study. DYC, CVC, DK, AHT, SA, NK, HLC, FD, and MS performed experiments. GL and MUG established and provided the modified CPER system. NAC, HPG, and AKO performed histopathologic and IHC analysis of mouse lungs. RNK generated the 3D image of spike. MCC and JZL performed sequencing analyses of recombinant viruses. DNK provided iPSC-derived alveolospheres. SCB and MB provided scientific input. AH and AE provided BAC harboring the SARS-CoV-2 genome. JHC provided the Omicron isolate. YK provided plasma samples. MS wrote the manuscript, which was read, edited, and approved by all authors.

COMPETING INTERESTS

RNK is an inventor on U.S. patent 10,960,070B2 entitled, "Prefusion coronavirus spike proteins and their use". MS is an inventor on a pending patent entitled, "Immunogenic compositions and use thereof" (USSN: 17/463,429). YK received unrelated funding from Abbott Laboratories to assess the durability of SARS-CoV-2 antibodies for healthcare workers. MB received funds from ARCA Biopharma for unrelated COVID-19 research. FD received funding from Moderna, Flagship Pioneering, and ARCA Biopharma for unrelated research. The remaining authors declare no competing interests.

EXTENDED DATA FIGURES

Extended Data Fig. 1: Schematic overview of mutations in Omicron S. Top panel shows amino acid changes in Omicron S compared to the SARS-CoV-2 Wuhan-Hu-1 isolate (NCBI

accession number: NC_045512). Numbering is based on Wuhan-Hu-1 sequence. Mutations not reported in previous variants of concern are shown in red. NTD, N-terminal domain; RBD, receptor-binding domain; RBM, receptor-binding motif. Bottom panel shows location of Omicron changes on the trimeric S protein. Domains are colored similarly in both panels.

Extended Data Fig. 2: Generating Recombinant SARS-CoV-2 by CPER. a, Schematic of recombinant SARS-CoV-2 generated by CPER (created with BioRender.com). S, spike; N, nucleocapsid. **b,** CPER protocol used in this study[24]. The SARS-CoV-2 genome was amplified into nine overlapping fragments. These fragments and a linker fragment (amplified from either pMW-CoV-2-UTRlinker or pGL-CPERlinker plasmid) were treated with PNK to phosphorylate 5' ends. The 5'-end- phosphorylated fragments were then stitched together by CPER, and the nicks in the resulting circular DNA molecule were closed by treatment with DNA ligase. The CPER product was transfected into cells to rescue virus particles. **c,** ACE2/TMPRSS2/Caco-2 cells transfected with the SARS-CoV-2 CPER product were stained with an anti-nucleocapsid antibody on indicated days post-transfection. DAPI was used to stain the cell nuclei. NC, negative control generated by omitting Fragment 9 from the CPER reaction. **d,** Virus titer in the culture medium of transfected cells at indicated days post-transfection, as measured by the plaque assay. The experiment was repeated twice. Individual values from both experiments are plotted.

Extended Data Fig. 3: Cytopathogenicity and replication of WT, Omi-S, and Omicron in ACE2/TMPRSS2/Caco-2 cells. a, Cell viability of SARS-CoV-2-infected ACE2/TMPRSS2/Caco-2 cells (MOI of 0.1) was quantified by the CellTiter-Glo assay at indicated times of infection. *P* values indicate a statistically significant difference between Omi-S and Omicron (n = 3 replicates). **b,** ACE2/TMPRSS2/Caco-2 cells were infected with WT, Omi-S, and Omicron at an MOI of 0.01, 0.1, or 1, and the viral titer in culture media was measured by the plaque assay at indicated times

post-infection. Statistically significant difference between Omi-S and Omicron has been shown for the middle time point (n = 3 replicates). *p* values were calculated by a two-tailed, unpaired *t*-test with Welch's correction. *p <0.05, **p <0.01, ***p <0.001, and ****p < 0.0001; ns, not significant.

Extended Data Fig. 4: Comparison of Omicron isolate and recombinant Omicron in cell culture. ACE2/TMPRSS2/Caco-2 (left) and Vero E6 (right) cells were infected with Omicron isolate or recombinant Omicron (generated by CPER) at an MOI of 0.01. The culture medium of infected cells was collected at indicated times, and the viral titer was measured by the plaque assay on ACE2/TMPRSS2/Caco-2 cells. The experiment was repeated twice, each time in three replicates. Error bars, mean ± SD (n = 3 replicates).

Extended Data Fig. 5: Spike cleavage and fusogenicity of Omi-S and Omicron. a, Western blot of S incorporated into virus particles. Virions generated in ACE2/TMPRSS2/Caco-2 cells were concentrated, and equal amount of total protein was loaded in each lane. S (antibody against S2 domain) and N were detected. Numbers at the bottom indicate mean ± SD of two independent experiments. **b,** S in infected cell lysates. ACE2/TMPRSS2/Caco-2 cells, infected at an MOI of 0.01, were harvested at 24 hpi and processed for Western blot with antibodies against S2 and nucleocapsid. β-actin served as an internal control. Numbers at the bottom indicate mean ± SD of two independent experiments. For gel source data, see Supplementary Fig. 2. **c**, Immunofluorescence staining of ACE2/TMPRSS2/293T cells with anti-nucleocapsid antibody. Nuclei was stained with DAPI. Infection was carried out at an MOI of 1 for 18h. Left, representative images; right, size of 20 syncytia from two experimental repeats. *p* values were calculated by a two-tailed, unpaired *t*-test with Welch's correction.

Extended Data Fig. 6: Preferential cell entry of Omi-S and Omicron through cathepsin-mediated pathway. Vero E6 or ACE2/TMPRSS2/Vero E6 cells treated with E64d for 2h were

infected at an MOI of 0.5 and stained with anti-nucleocapsid antibody at 24 hpi for IF analysis. Bar graphs show percentage of infected cells relative to DMSO control, for which the values were arbitrarily set at 100. Error bars, mean ± SD (n = 4 replicates). The experiment was performed only once. *p* values were calculated by a two-tailed, unpaired *t* test with Welch's correction.

Extended Data Fig. 7: Clinical signs in Omi-S-infected mice. K18-hACE2 mice (*n = 10*) inoculated intranasally with 1 x 10^4 PFU of Omi-S and described in Fig. 2a-c were monitored for body weight (**a**) and clinical score (**b**). Animals losing 20% of their body weight (8 out of 10) were euthanized. The surviving animals did not show any signs of distress.

Extended Data Fig. 8: Lung pathology and nasal turbinate IHC in mice infected with WT, Omi-S, and Omicron. The lungs and nasal turbinates of K18-hACE2 mice intranasally inoculated with 1 x 10^4 PFU of WT, Omi-S, and Omicron were collected at 2 dpi for histological analysis. **a,** Representative images of hematoxylin and eosin (H&E) staining for the detection of bronchiolar damage in the lungs of the infected mice. The bronchiolar epithelial necrosis is shown with arrows. **b,** IHC staining to detect SARS-CoV-2 S protein in the same area where bronchiolar necrosis was seen. No evidence of necrosis was found in bronchioles of mice infected with Omicron. (Scale bar = 100 µm). **c,** Nucleocapsid distribution and abundance in the nasal passages of WT, Omi-S, and Omicron. Left, representative images; Right, N-immunoreactivity in nasal respiratory epithelium presented as percentage of the mean of WT (n = 2 mice for WT and Omicron; n = 3 mice for Omi-S). Chromogenic 3,3'-Diaminobenzidine (DAB) immunohistochemistry: (left panel, 12.5x total magnification; right panel, 400x total magnification). Higher magnification views of nasal respiratory epithelium indicated by red squares are shown on right. Scale bars; left panel, 800 microns; right panel, 20 microns.

Extended Data Fig. 9: Panel of chimeric viruses containing spike and non-spike mutations. **a,** Amino acid changes outside of S in Omicron BA.1 compared to D614-containing ancestral SARS-CoV-2. Proteins with amino acid changes are shown in red, whereas wild-type proteins are in blue. Amino acid numbers are according to individual viral proteins. **b,** Schematic representation of recombinant viruses generated by CPER. ORF7a was being replaced with mNeonGreen to generate reporter viruses. *Sequencing analysis showed that Omi-S/M lacked the A63T mutation in M, despite it being present in the plasmid used for CPER. S, spike; E, envelope; M, membrane; N, nucleocapsid.

Extended Data Fig. 10: Individual neutralization data. Individual neutralization curves for the data presented in Fig. 4a,b are shown. The data represent the mean ± SD of three technical replicates. The curves were calculated based on a non-linear regression curve fit analysis in Prism. The dotted lines represent the limit of detection.

Extended Data Table 1: Information about serum samples. Overview of serum samples used for the analysis of antibody neutralization of WA1, Omi-S, and Omicron. *Days after the second vaccine shot. **The spike antibody titer was measured by Abbott's SARS-CoV-2 immunoassays.

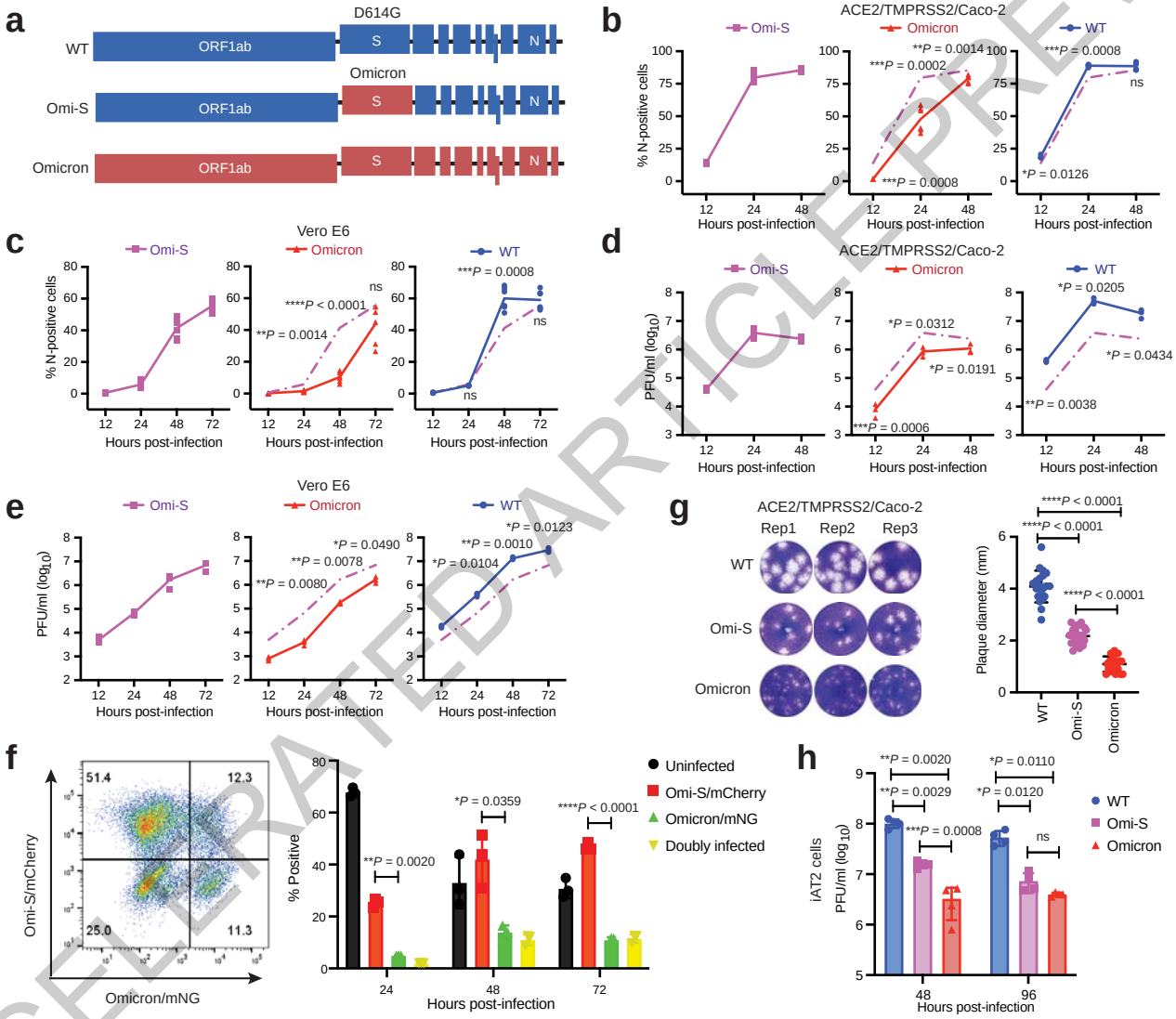

Fig. 2

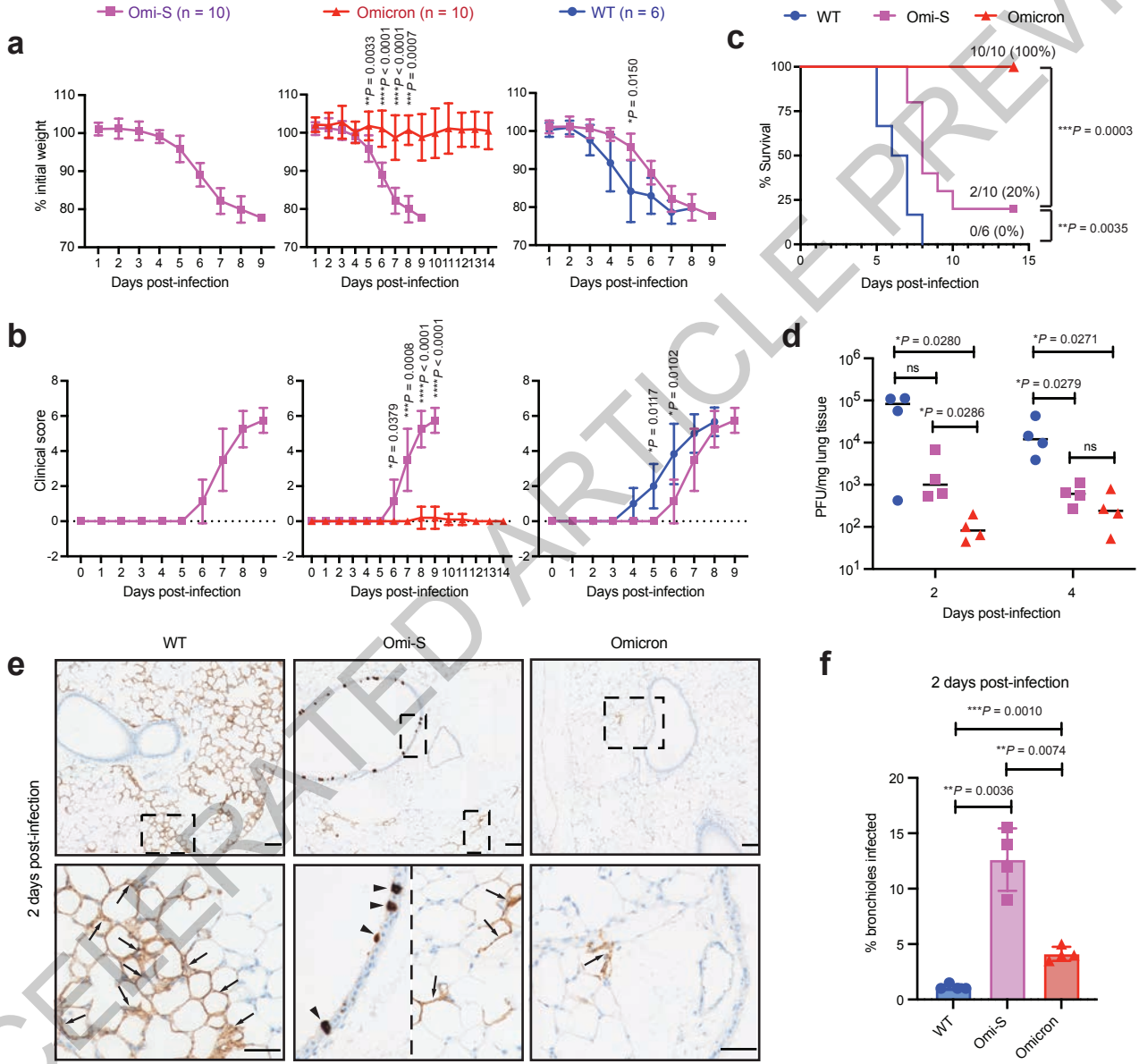

Fig. 3

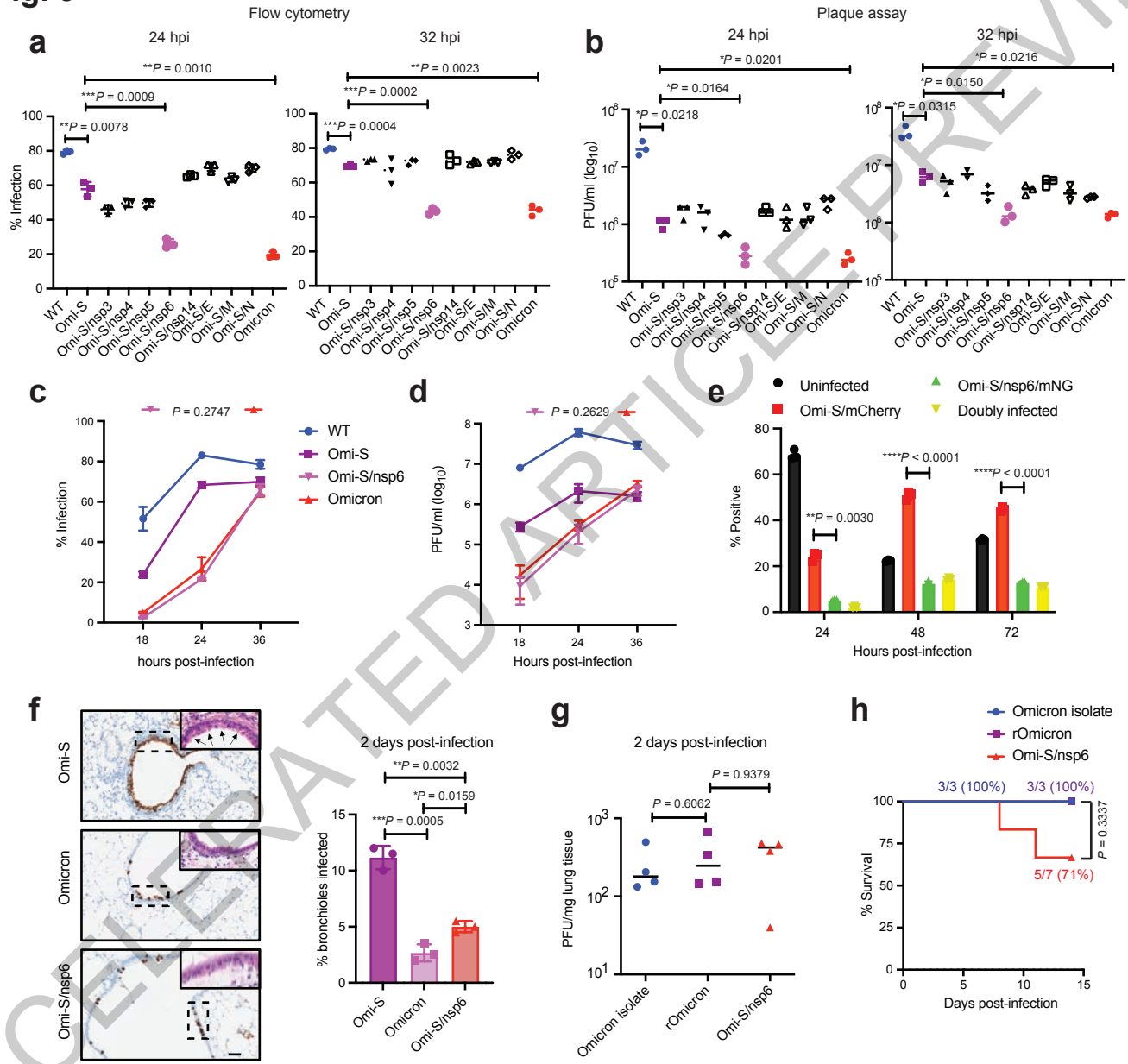

Fig. 4

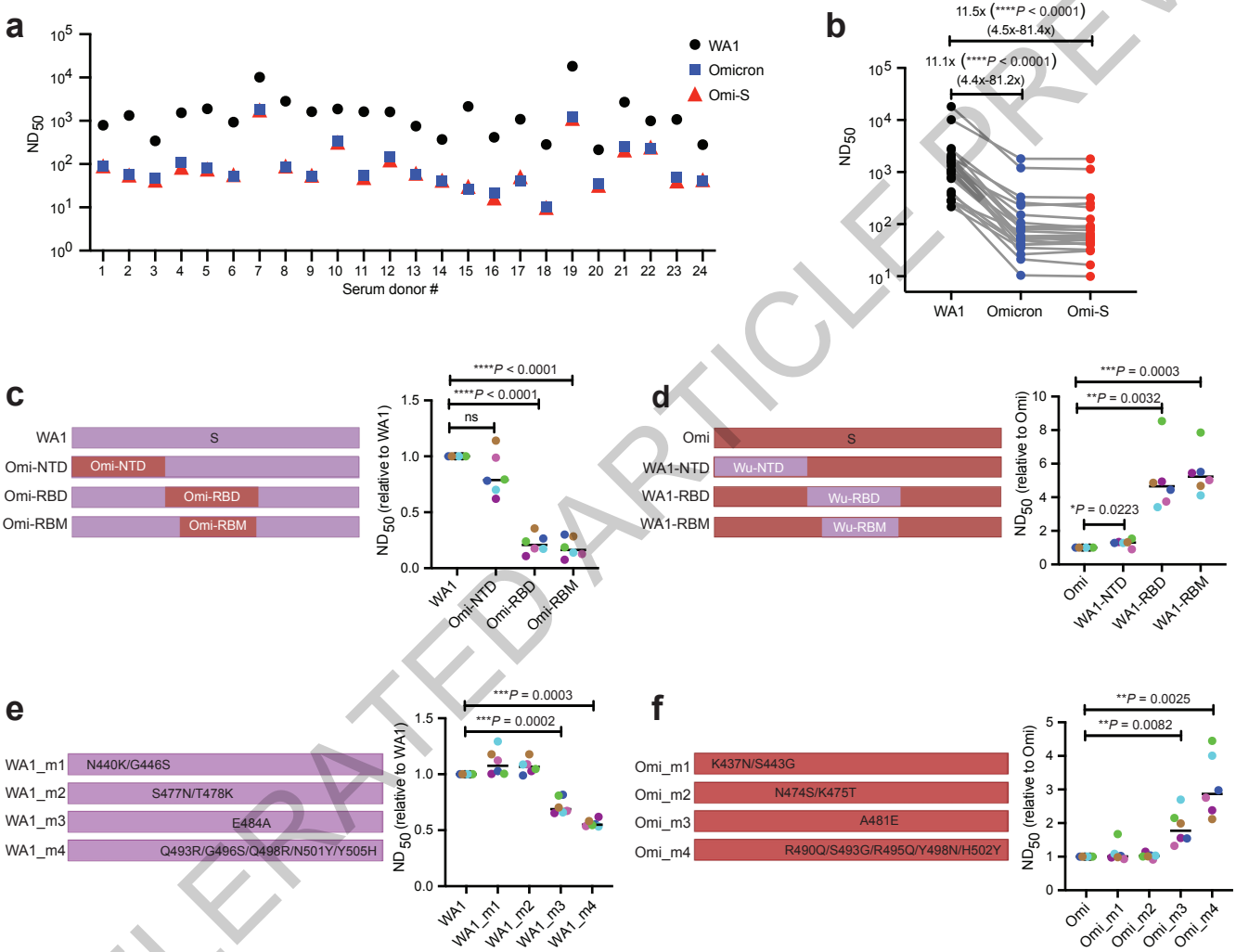

Extended Data Fig. 1

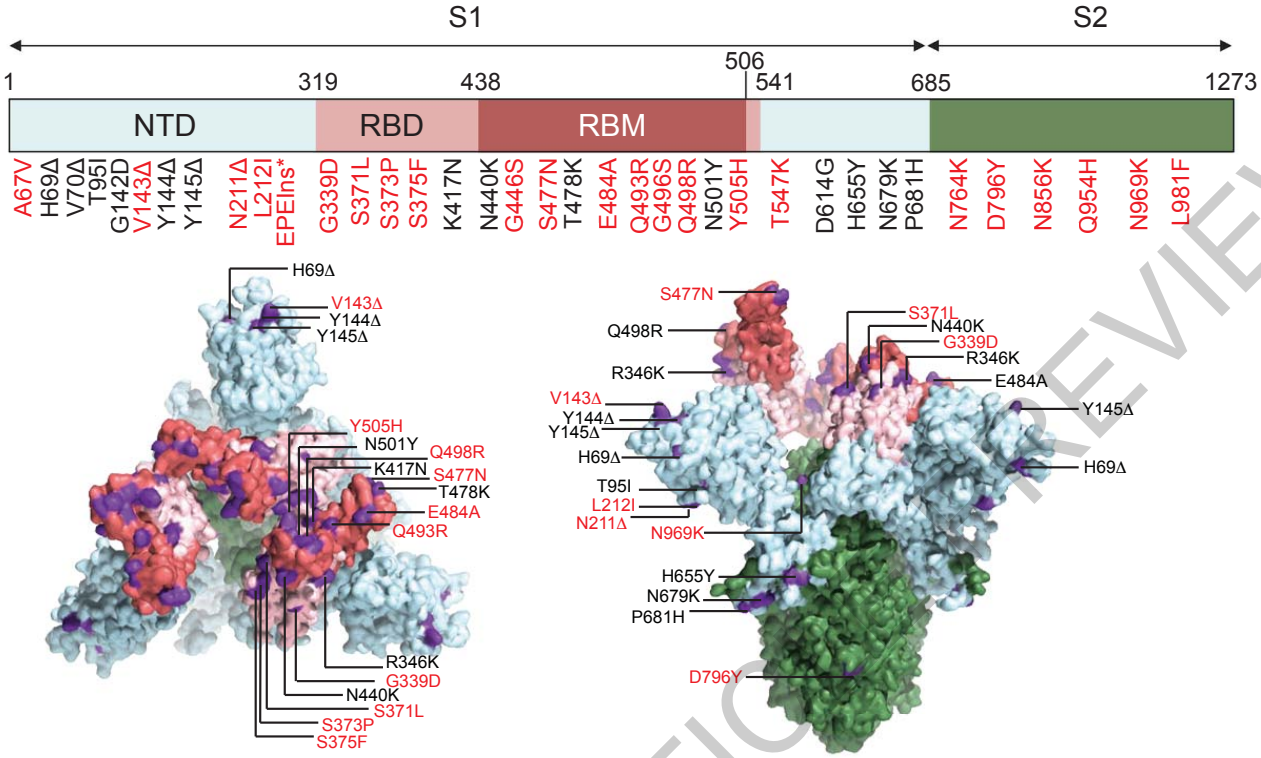

Extended Data Fig. 2

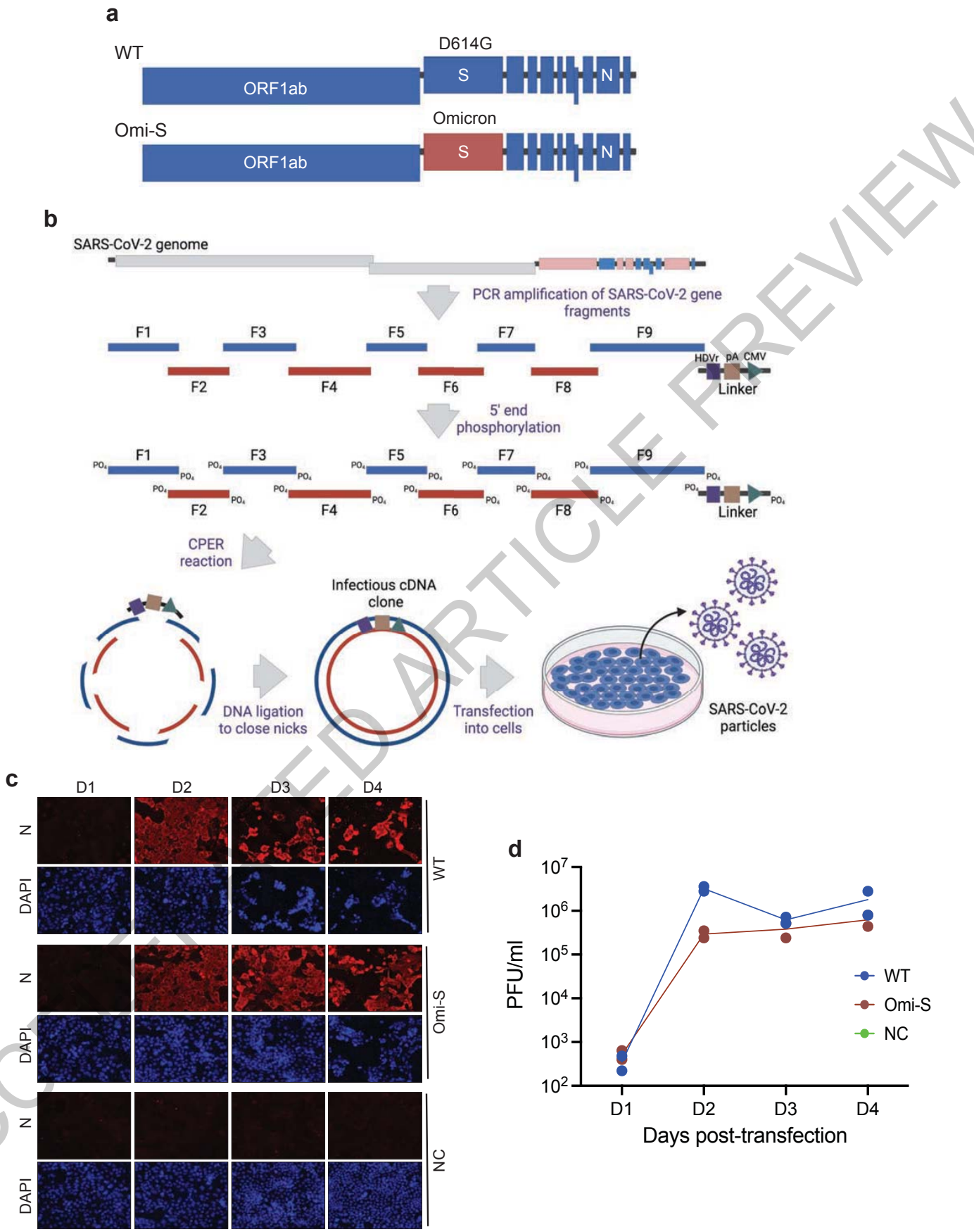

Extended Data Fig. 3

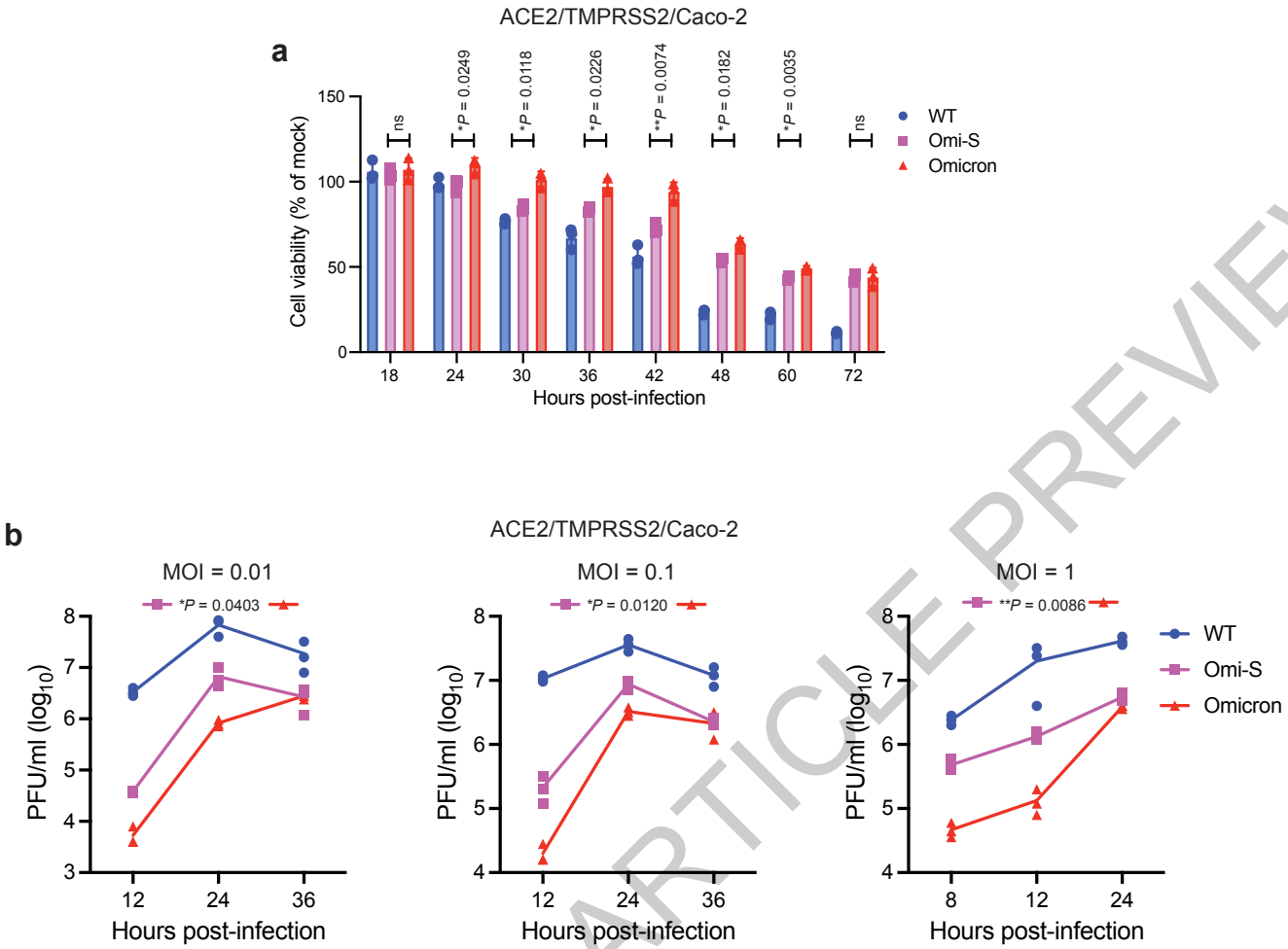

Extended Data Fig. 4

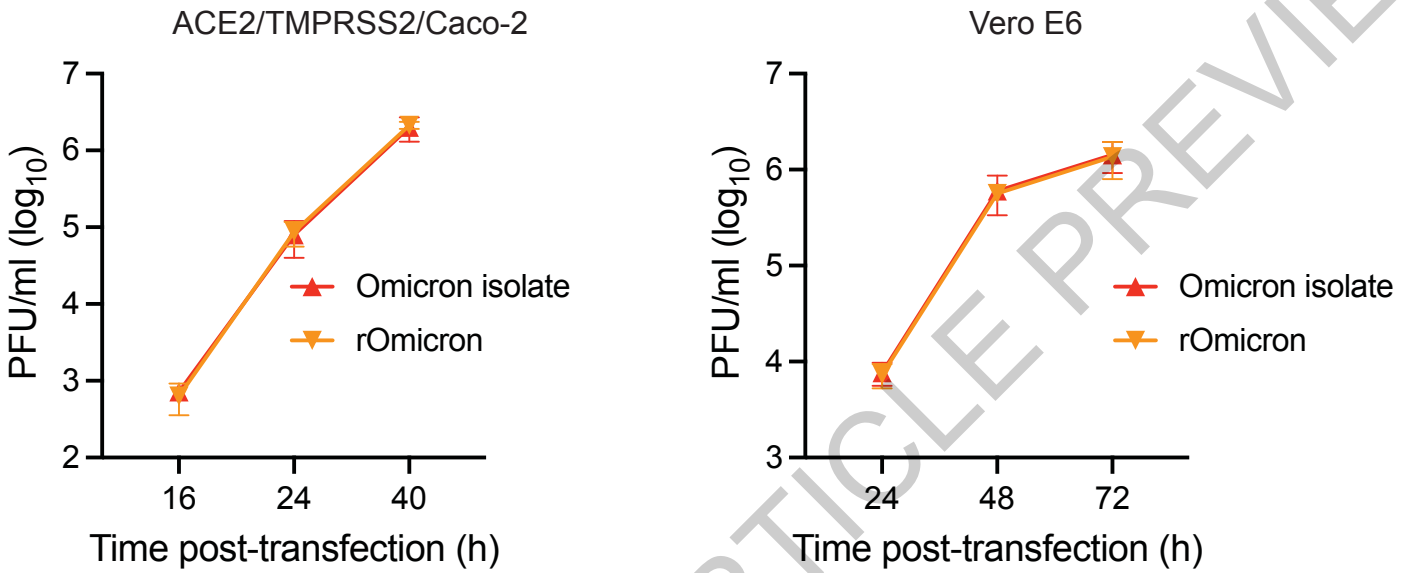

Extended Data Fig. 5

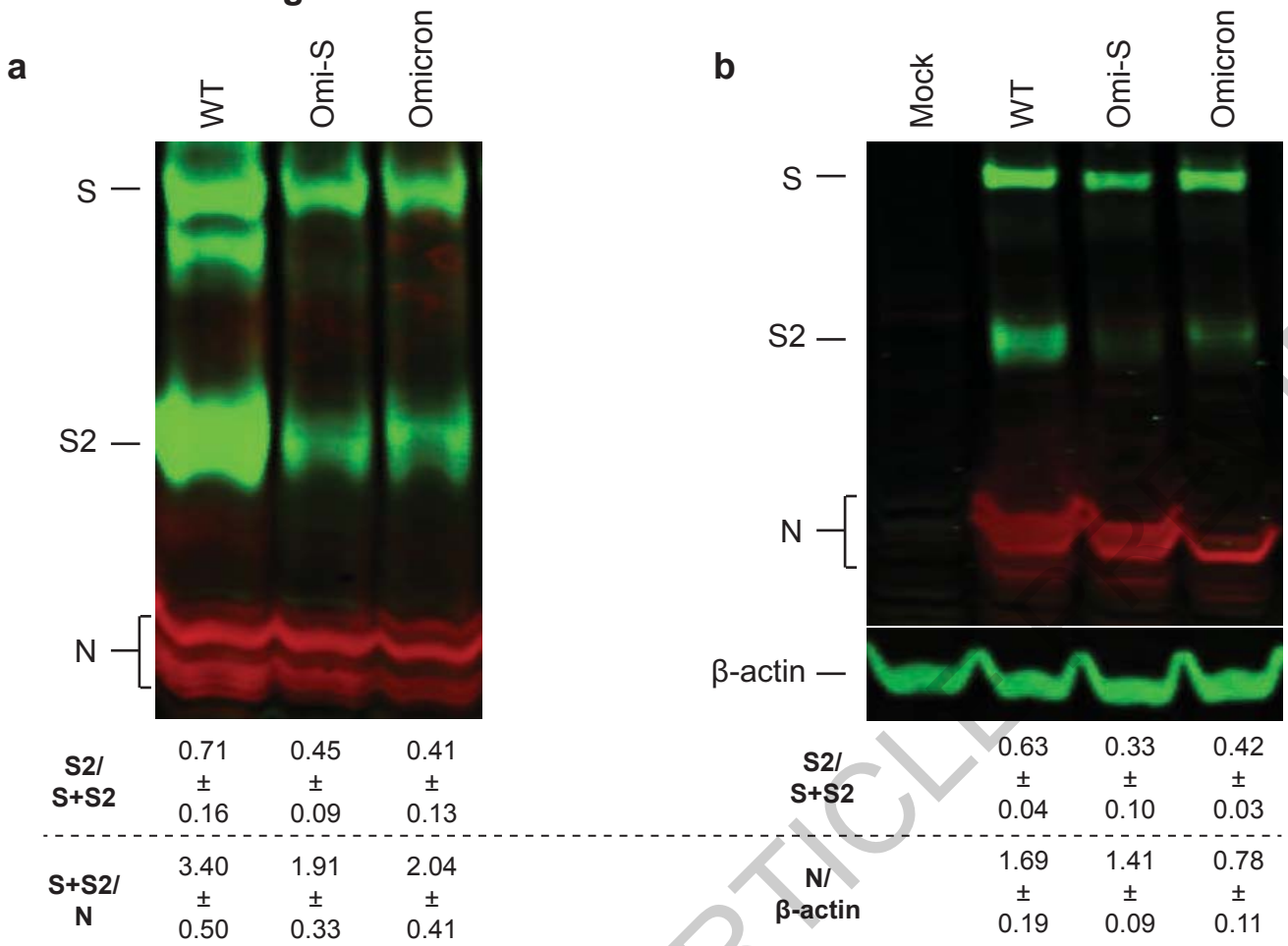

	WT	Omi-S	Omicron
S2/S+S2	0.71 ± 0.16	0.45 ± 0.09	0.41 ± 0.13
S+S2/N	3.40 ± 0.50	1.91 ± 0.33	2.04 ± 0.41

	Mock	WT	Omi-S	Omicron
S2/S+S2	0.63 ± 0.04	0.33 ± 0.10	0.42 ± 0.03	
N/β-actin	1.69 ± 0.19	1.41 ± 0.09	0.78 ± 0.11	

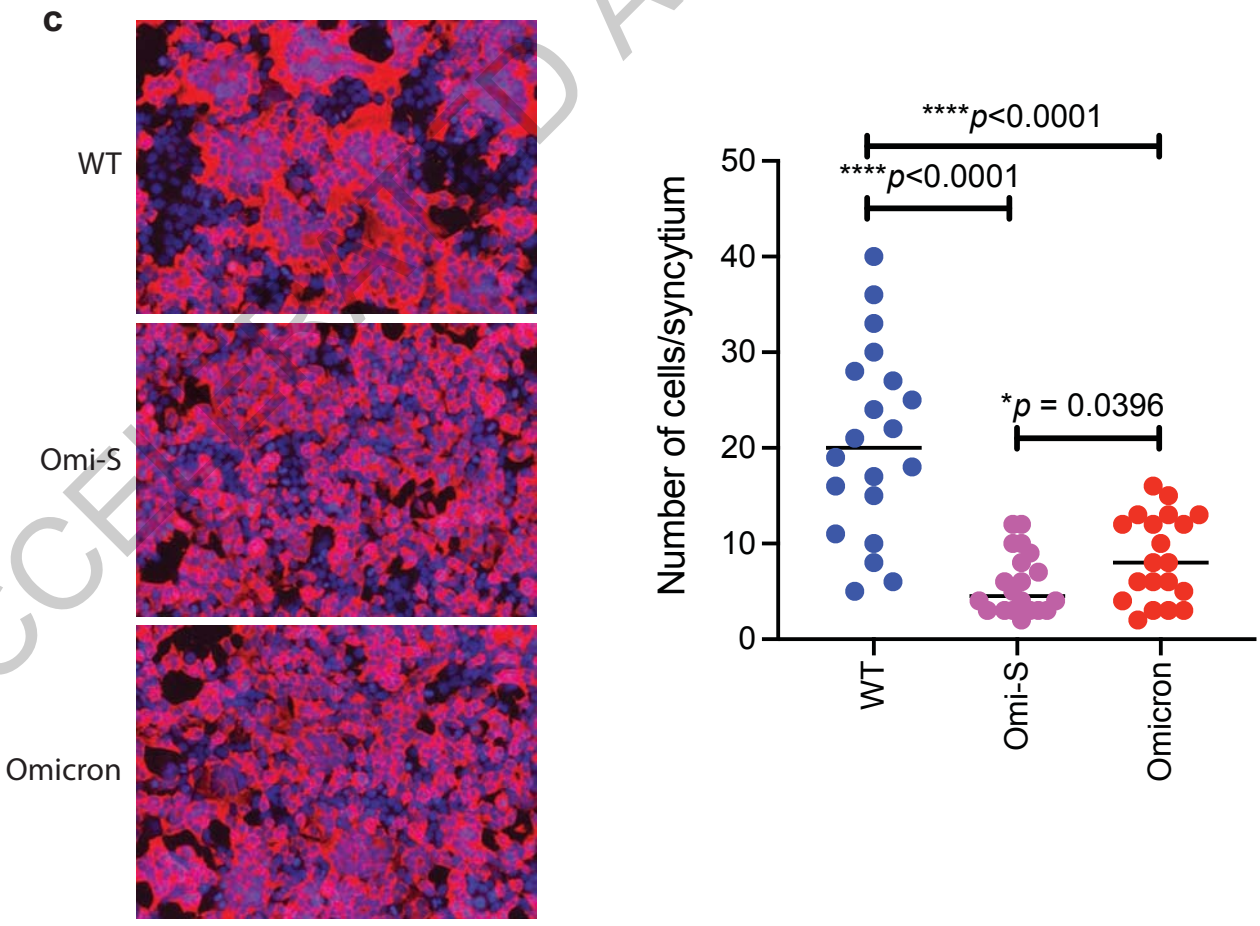

Extended Data Fig. 6

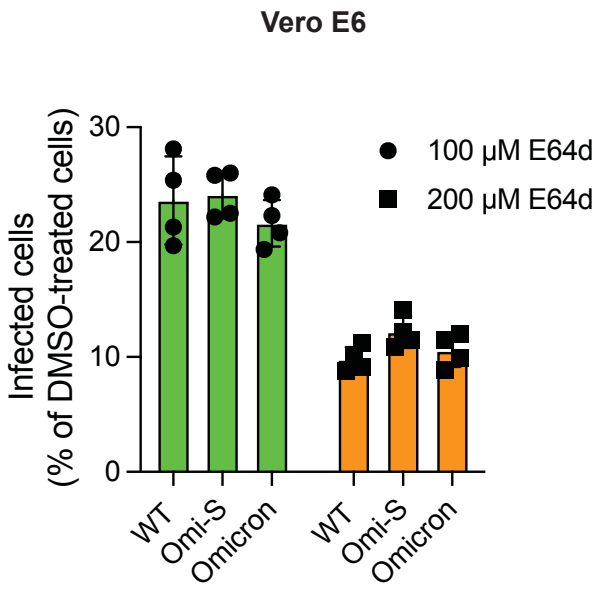

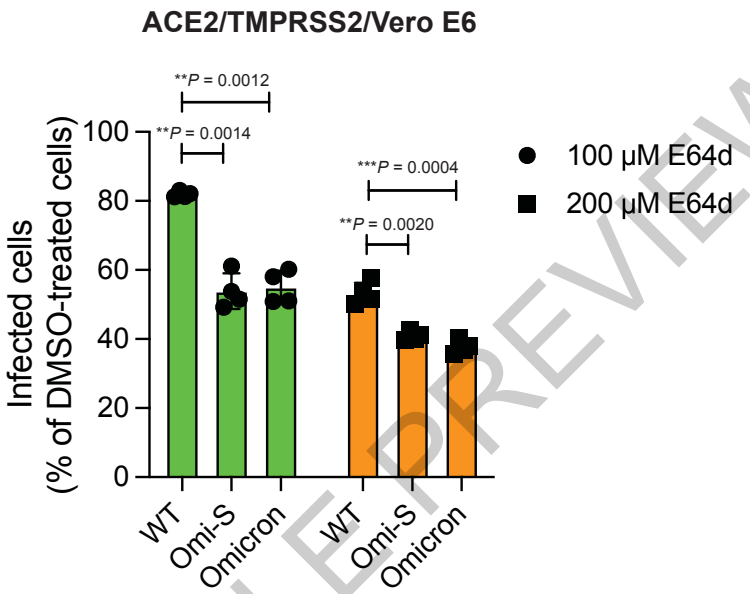

Extended Data Fig. 7

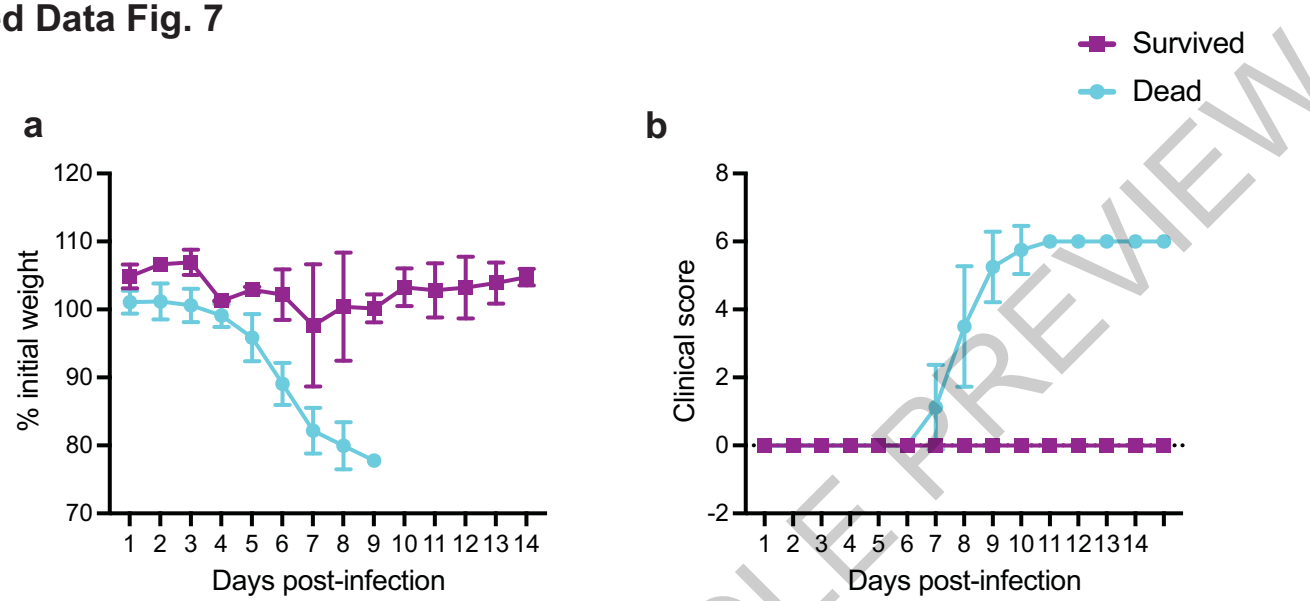

Extended Data Fig. 8

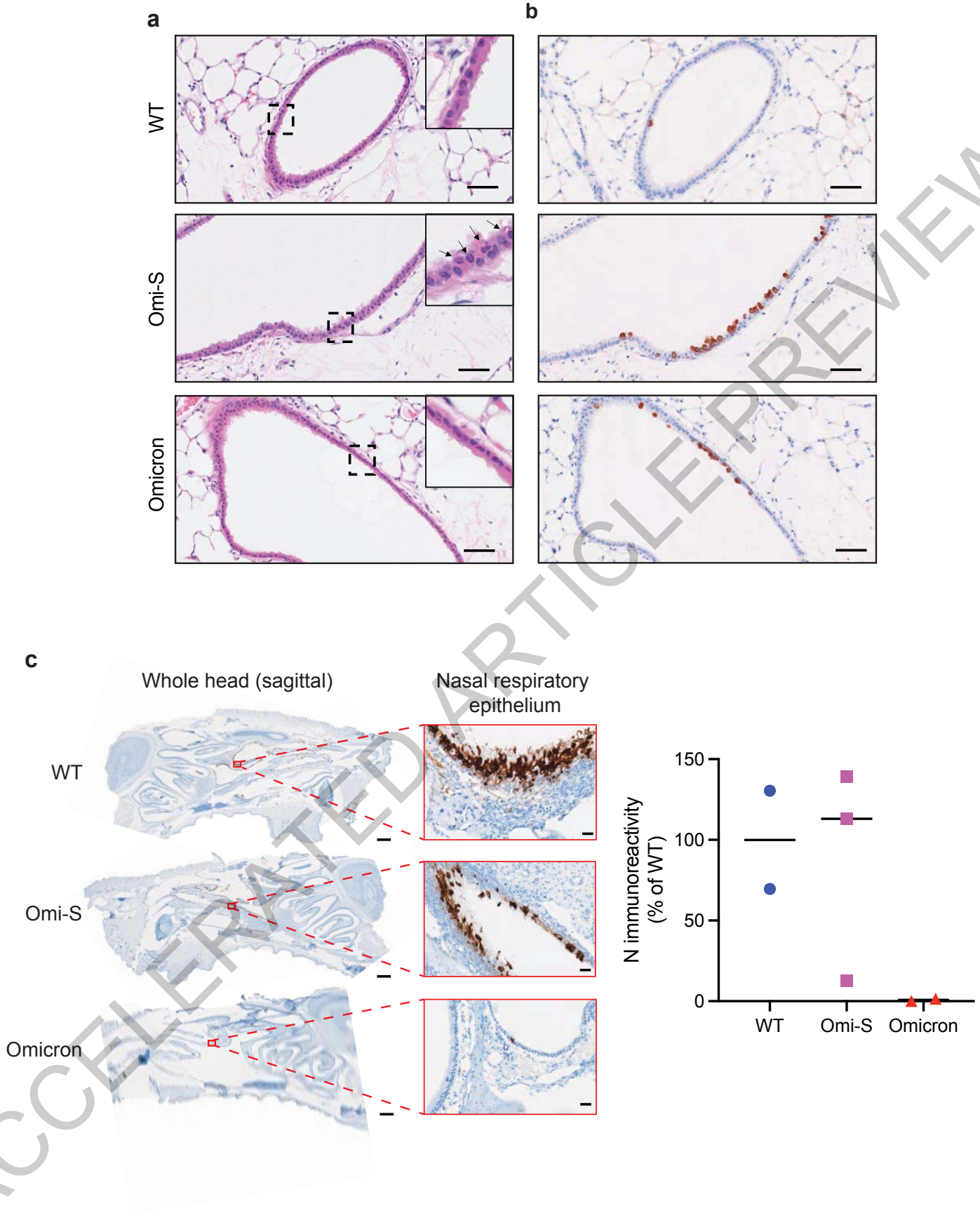

Extended Data Fig. 9

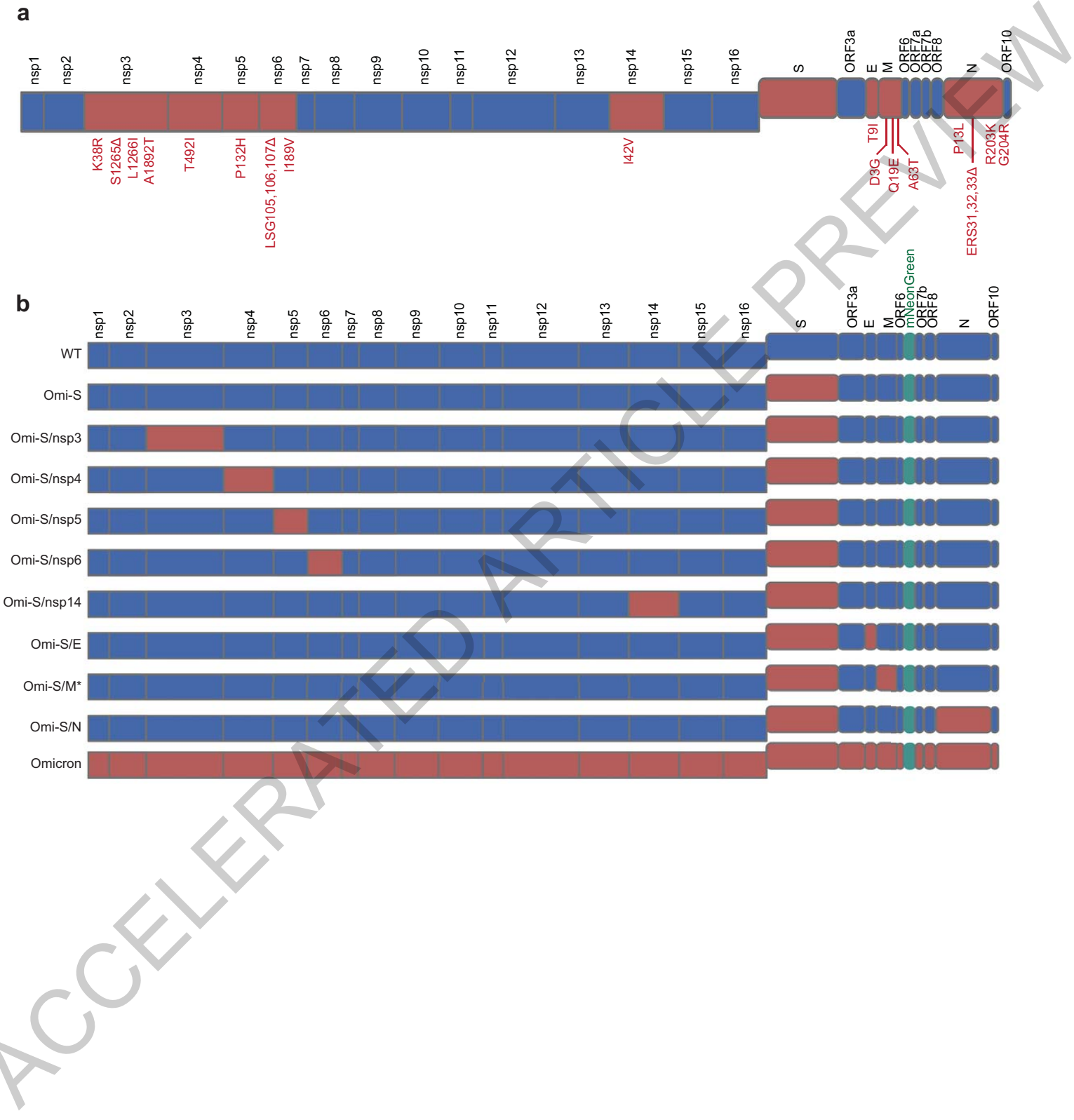

Extended Data Fig. 10

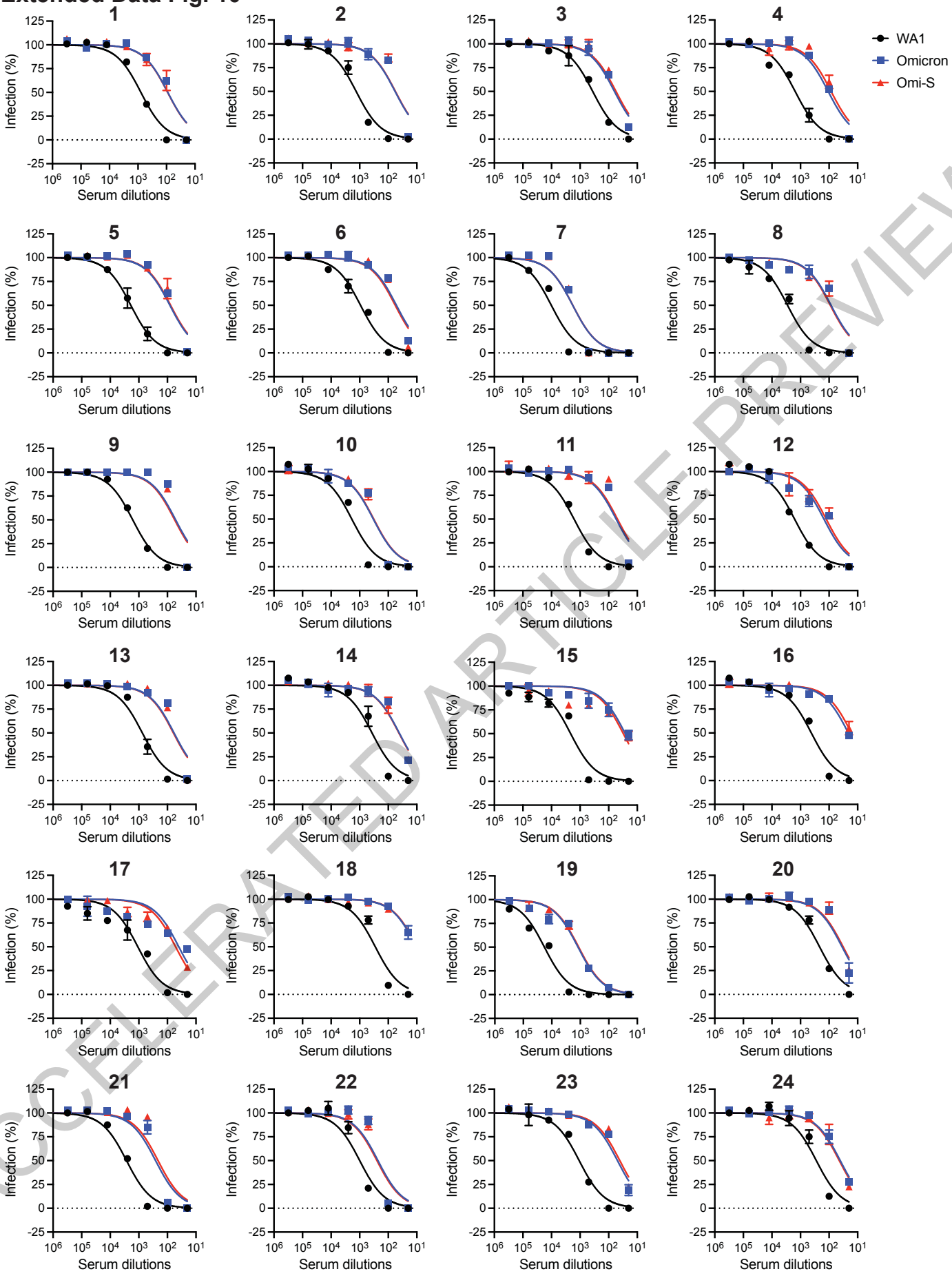

Extended Data Table 1

Serum no.	Sex	Race	Age	Days post-vaccination*	Vaccine (Manufacturer)	Spike Ab titer (AU/ml)**
1	Male	White	59	18	mRNA-1273 (Moderna)	39823.0
2	Male	Black	26	37	mRNA-1273 (Moderna)	26978.7
3	Male	Asian	55	34	mRNA-1273 (Moderna)	24880.7
4	Male	White	39	32	mRNA-1273 (Moderna)	23816.7
5	Male	Asian	45	38	mRNA-1273 (Moderna)	21659.5
6	Male	White	30	32	mRNA-1273 (Moderna)	18986.5
7	Female	Asian	47	35	mRNA-1273 (Moderna)	100000.0
8	Female	White	62	47	mRNA-1273 (Moderna)	69680.0
9	Female	White	39	14	mRNA-1273 (Moderna)	54996.6
10	Female	White	38	32	mRNA-1273 (Moderna)	46494.7
11	Female	White	34	30	mRNA-1273 (Moderna)	43784.0
12	Female	White	57	42	mRNA-1273 (Moderna)	42140.5
13	Male	Mixed	28	51	BNT162b2 (Pfizer-BioNTech)	17623.8
14	Male	White	30	54	BNT162b2 (Pfizer-BioNTech)	16154.5
15	Male	White	29	54	BNT162b2 (Pfizer-BioNTech)	14261.5
16	Male	Asian	48	48	BNT162b2 (Pfizer-BioNTech)	10593.6
17	Male	White	46	60	BNT162b2 (Pfizer-BioNTech)	9752.3
18	Male	White	31	53	BNT162b2 (Pfizer-BioNTech)	8715.2
19	Female	White	55	52	BNT162b2 (Pfizer-BioNTech)	100000.0
20	Female	White	43	47	BNT162b2 (Pfizer-BioNTech)	44385.4
21	Female	White	56	48	BNT162b2 (Pfizer-BioNTech)	39998.5
22	Female	Mixed	44	49	BNT162b2 (Pfizer-BioNTech)	31141.9
23	Female	White	56	50	BNT162b2 (Pfizer-BioNTech)	25969.6
24	Female	White	55	51	BNT162b2 (Pfizer-BioNTech)	23539.1

nature portfolio

Corresponding author(s): Mohsan Saeed

Last updated by author(s): November 30, 2022

Reporting Summary

Nature Portfolio wishes to improve the reproducibility of the work that we publish. This form provides structure for consistency and transparency in reporting. For further information on Nature Portfolio policies, see our Editorial Policies and the Editorial Policy Checklist.

Statistics

For all statistical analyses, confirm that the following items are present in the figure legend, table legend, main text, or Methods section.

n/a	Confirmed	
☐	☒	The exact sample size (*n*) for each experimental group/condition, given as a discrete number and unit of measurement
☐	☒	A statement on whether measurements were taken from distinct samples or whether the same sample was measured repeatedly
☐	☒	The statistical test(s) used AND whether they are one- or two-sided *Only common tests should be described solely by name; describe more complex techniques in the Methods section.*
☒	☐	A description of all covariates tested
☒	☐	A description of any assumptions or corrections, such as tests of normality and adjustment for multiple comparisons
☐	☒	A full description of the statistical parameters including central tendency (e.g. means) or other basic estimates (e.g. regression coefficient) AND variation (e.g. standard deviation) or associated estimates of uncertainty (e.g. confidence intervals)
☐	☒	For null hypothesis testing, the test statistic (e.g. *F*, *t*, *r*) with confidence intervals, effect sizes, degrees of freedom and *P* value noted *Give P values as exact values whenever suitable.*
☒	☐	For Bayesian analysis, information on the choice of priors and Markov chain Monte Carlo settings
☒	☐	For hierarchical and complex designs, identification of the appropriate level for tests and full reporting of outcomes
☒	☐	Estimates of effect sizes (e.g. Cohen's *d*, Pearson's *r*), indicating how they were calculated

Our web collection on statistics for biologists contains articles on many of the points above.

Software and code

Policy information about availability of computer code

Data collection	No software was used for data collection
Data analysis	GraphPad Prism Version 9.4.1 was used to perform statistical analyses. FlowJo Version was used to analyze the flow cytometry data.

For manuscripts utilizing custom algorithms or software that are central to the research but not yet described in published literature, software must be made available to editors and reviewers. We strongly encourage code deposition in a community repository (e.g. GitHub). See the Nature Portfolio guidelines for submitting code & software for further information.

Data

Policy information about availability of data

All manuscripts must include a data availability statement. This statement should provide the following information, where applicable:

- Accession codes, unique identifiers, or web links for publicly available datasets
- A description of any restrictions on data availability
- For clinical datasets or third party data, please ensure that the statement adheres to our policy

All data supporting the conclusions of this study are reported in the paper. The raw data are available from the corresponding author with no restrictions upon reasonable request.

Human research participants

Policy information about studies involving human research participants and Sex and Gender in Research.

Reporting on sex and gender	N/A
Population characteristics	N/A
Recruitment	N/A
Ethics oversight	N/A

Note that full information on the approval of the study protocol must also be provided in the manuscript.

Field-specific reporting

Please select the one below that is the best fit for your research. If you are not sure, read the appropriate sections before making your selection.

☒ Life sciences ☐ Behavioural & social sciences ☐ Ecological, evolutionary & environmental sciences

For a reference copy of the document with all sections, see nature.com/documents/nr-reporting-summary-flat.pdf

Life sciences study design

All studies must disclose on these points even when the disclosure is negative.

Sample size	In vitro studies: No sample-size calculation was performed a priori. All experiments with statistical analyses were repeated at least twice, each with multiple technical replicates. In vivo studies: Cohort sizes were determined based on our previous SARS-CoV-2 studies in animals (PMID: 35336942) and others' animal studies (PMID: 35062015). We used n=7-10 for death/survival studies, n=4 for monitoring viral load in the lung of infected animals, and n= 2 or 3 for IHC.
Data exclusions	No data were excluded from the analyses.
Replication	Each experiment was repeated at least twice and the results were successfully reproduced. To confirm the authenticity of our results, we repeated our experiments with independently generated virus stocks.
Randomization	There are no experimental groups in our study, so this does not apply.
Blinding	There are no group allocations in this study, so this does not apply.

Reporting for specific materials, systems and methods

We require information from authors about some types of materials, experimental systems and methods used in many studies. Here, indicate whether each material, system or method listed is relevant to your study. If you are not sure if a list item applies to your research, read the appropriate section before selecting a response.

Materials & experimental systems

n/a	Involved in the study
☐	☒ Antibodies
☐	☒ Eukaryotic cell lines
☒	☐ Palaeontology and archaeology
☐	☒ Animals and other organisms
☐	☐ Clinical data
☒	☐ Dual use research of concern

Methods

n/a	Involved in the study
☒	☐ ChIP-seq
☐	☒ Flow cytometry
☒	☐ MRI-based neuroimaging

Antibodies

Antibodies used	For flow cytometry: Rabbit anti-SARS-CoV nucleocapsid polyclonal antibody (Rockland; #200-401-A50; 1:1000) Donkey anti-Rabbit IgG-AF647 secondary antibody (ThermoFisher Scientific; #A-31573; 1:1000)

For IF:
Rabbit anti-SARS-CoV nucleocapsid polyclonal antibody (Rockland; #200-401-A50; 1:2000)
Alexa Fluor 568-conjugated goat anti-Rabbit secondary antibody (Invitrogen; #A11008; 1:1000)

For IHC:
Mouse anti-SARS-CoV nuceocapsid monoclonal antibody (Cell Signaling Technologies; #68344; 1:1000) (For the SARS-CoV-2 N antibody, given its mouse origin, an additional rabbit anti-mouse anti-Ig1 + Ig2a + IgG3 antibody (Abcam; #133469; 1:1000) was used to prevent non-specific binding.)
Anti-SARS-CoV-2 spike protein (S1) antibody (Cell Signaling Technology; # 99423; 1:400)

For Western Blot:
Rabbit anti-SARS-CoV nucleocapsid polyclonal antibody (Rockland; #200-401-A50; 1:1000)
Mouse anti-SARS-CoV-2 spike monoclonal antibody (GeneTex; #GTX632604; 1:1000)
IRDye 800CW Donkey anti-Mouse IgG secondary antibody (LI-COR Biosciences; #926-32212; 1:5000)
IRDye 680RD Donkey anti-Rabbit IgG secondary antibody (LI-COR Biosciences; #926-68073; 1:5000)

Validation

Rabbit anti-SARS-CoV nucleocapsid polyclonal antibody (Rockland; #200-401-A50; 1:1000)
Mouse anti-SARS-CoV nuceocapsid monoclonal antibody (Cell Signaling Technologies; #68344; 1:1000)
Anti-SARS-CoV-2 spike protein (S1) antibody (Cell Signaling Technology; # 99423; 1:400)
Rabbit anti-SARS-CoV nucleocapsid polyclonal antibody (Rockland; #200-401-A50; 1:1000)
Mouse anti-SARS-CoV-2 spike monoclonal antibody (GeneTex; #GTX632604; 1:1000)
These antibodies were validated using uninfected cells as negative controls. No signal was obtained in uninfected cells.

Donkey anti-Rabbit IgG-AF647 secondary antibody (ThermoFisher Scientific; #A-31573; 1:1000)
Alexa Fluor 568-conjugated goat anti-Rabbit secondary antibody (Invitrogen; #A11008; 1:1000)
IRDye 800CW Donkey anti-Mouse IgG secondary antibody (LI-COR Biosciences; #926-32212; 1:5000)
IRDye 680RD Donkey anti-Rabbit IgG secondary antibody (LI-COR Biosciences; #926-68073; 1:5000)
These are secondary antibodies extensively validated by the providers for flow cytometry, IF, and western blot. As described in the Method section, these antibodies worked optimally with our protocols.

Eukaryotic cell lines

Policy information about cell lines and Sex and Gender in Research

Cell line source(s)	Human embryonic kidney HEK293T cells (ATCC; CRL-3216), human lung adenocarcinoma A549 cells (ATCC; CCL-185), African green monkey kidney Vero E6 cells, and human colorectal adenocarcinoma Caco-2 cells (ATCC; HTB-37), and human induced pluripotent stem cell-derived alveolar type 2 epithelial cells.
Authentication	None of the cell lines was authenticated.
Mycoplasma contamination	All cell types described were regularly tested and found to be mycoplasma-free.
Commonly misidentified lines (See ICLAC register)	No commonly misidentified cell lines were used in this study.

Animals and other research organisms

Policy information about studies involving animals; ARRIVE guidelines recommended for reporting animal research, and Sex and Gender in Research

Laboratory animals	Heterozygous K18-hACE2 C57BL/6J mice (Strain 2B6.Cg-Tg(K18-ACE2)2Prlmn/J) were purchased from the Jackson Laboratory (Jax, Bar Harbor, ME). Both male and female mice in the age range of 12-20 weeks were being used. Mice were housed in groups of 4 to 5 and maintained on a 12:12 light cycle at 30-70% humidity and 68F temperature. The mice were provided water and standard chow diet (LabDiet, St. Louis, MO, USA) ad libitum.
Wild animals	No wild animals were used in this study.
Reporting on sex	Both male and female mice in the age range of 12-20 weeks were being used.
Field-collected samples	No field collected samples were used.
Ethics oversight	Animal studies were performed following the recommendations in the Guide for the Care and Use of Laboratory Animals of the National Institutes of Health. The protocols were approved by the Boston University Institutional Animal Care and Use Committee (IACUC).

Note that full information on the approval of the study protocol must also be provided in the manuscript.

Clinical data

Policy information about clinical studies

All manuscripts should comply with the ICMJE guidelines for publication of clinical research and a completed CONSORT checklist must be included with all submissions.

Clinical trial registration	*Provide the trial registration number from ClinicalTrials.gov or an equivalent agency.*
Study protocol	*Note where the full trial protocol can be accessed OR if not available, explain why.*
Data collection	*Describe the settings and locales of data collection, noting the time periods of recruitment and data collection.*
Outcomes	*Describe how you pre-defined primary and secondary outcome measures and how you assessed these measures.*

Flow Cytometry

Plots

Confirm that:

☒ The axis labels state the marker and fluorochrome used (e.g. CD4-FITC).

☒ The axis scales are clearly visible. Include numbers along axes only for bottom left plot of group (a 'group' is an analysis of identical markers).

☒ All plots are contour plots with outliers or pseudocolor plots.

☒ A numerical value for number of cells or percentage (with statistics) is provided.

Methodology

Sample preparation	For flow cytometry, fixed cells were permeabilized in 1x permeabilization buffer (ThermoFisher Scientific; #00-5523-00) and stained with SARS-CoV-2 nucleocapsid antibody (Rockland; #200-401-A50), followed by donkey anti-rabbit IgG-AF647 secondary antibody (ThermoFisher Scientific; #A-31573). Gating was based on uninfected stained control cells. The extent of staining was quantified using a BD LSR II flow cytometer (BD Biosciences, CA), and the data were analyzed with FlowJo v10.6.2 (FlowJo, Tree Star Inc). For some experiments, we used fluorescently labeled viruses. In these cases, fixed cells were permeabilized in 1x permeabilization buffer (ThermoFisher Scientific; #00-5523-00) and subjected to flow cytometry. Gating was based on uninfected stained control cells. Where needed, single-color cells were used as controls. The extent of staining was quantified using a BD LSR II flow cytometer (BD Biosciences, CA), and the data were analyzed with FlowJo v10.6.2 (FlowJo, Tree Star Inc).
Instrument	LSR-II
Software	FlowJo
Cell population abundance	Since we worked only with the cell lines, we did not determine the purity of cells.
Gating strategy	The FSC/SSC gates were applied, before the cells were separated into SARS-CoV-2 positive and negative cell populations. When dealing with cells infected with two distinctly-colored viruses, we used single-color cells as controls.

☒ Tick this box to confirm that a figure exemplifying the gating strategy is provided in the Supplementary Information.